Graduate School ETD Form 9
(Revised 01/14)

PURDUE UNIVERSITY
GRADUATE SCHOOL
Thesis/Dissertation Acceptance

This is to certify that the thesis/dissertation prepared

By Yi Zhang

Entitled
Atomistic and Finite Element Modeling of Zirconia for Thermal Barrier Coating Applications

For the degree of Master of Science in Mechanical Engineering

Is approved by the final examining committee:

Jing Zhang

Hazim El-Mounaryi

Andres Tovar

To the best of my knowledge and as understood by the student in the *Thesis/Dissertation Agreement. Publication Delay, and Certification/Disclaimer (Graduate School Form 32)*, this thesis/dissertation adheres to the provisions of Purdue University's "Policy on Integrity in Research" and the use of copyrighted material.

Approved by Major Professor(s): Jing Zhang

Approved by: Sohel Anwar 07/03/2014

Head of the Department Graduate Program Date

ATOMISTIC AND FINITE ELEMENT MODELING OF ZIRCONIA FOR THERMAL BARRIER COATING APPLICATIONS

A Thesis

Submitted to the Faculty

of

Purdue University

by

Yi Zhang

In Partial Fulfillment of the

Requirements for the Degree

of

Master of Science in Mechanical Engineering

August 2014

Purdue University

Indianapolis, Indiana

ACKNOWLEDGMENTS

I would like to thank my advisor, Professor Jing Zhang, for his guidance, encouragement, support, and patience during the entire course of this research and thesis work. He is always willing to provide me help and guidance to move the research forward.

I would also like to thank Professor Hazim El-Mounaryi and Professor Andres Tovar for serving on my thesis committee and for their valuable comments. Also thank Professor Yeon-Gil Jung at the Changwon National University and Dr. Li Li at Praxair Surface Technologies for their suggestions.

I would like to extend my special thanks to Dr. Jing Zhangs research group members, including Ph.D. candidates Linmin Wu and Xingye Guo, in the discussions with them, many problems during my thesis research are solved. I am also in great debt to Jiayang Liu for his help in the lab and brilliant comments on my thesis.

I would also like to thank Ms. Valerie Lim Diemer for assisting me in formatting this thesis. I am grateful for the people from the Mechanical Engineering department, my friends, Lujie, Weng-Hoh and many more. Without them, graduate life would have never been the same. Finally, I express my gratitude to my parents for their support and encouragement during my life.

TABLE OF CONTENTS

LIST OF TABLES

LIST OF FIGURES

Figure Page

ABSTRACT

Zhang, Yi. M.S.M.E., Purdue University, August 2014. Atomistic and Finite Element Modeling of Zirconia for Thermal Barrier Coating Applications. Major Professor: Jing Zhang, School of Mechanical Engineering.

Zirconia (ZrO_2) is an important ceramic material with a broad range of applications. Due to its high melting temperature, low thermal conductivity, and high-temperature stability, zirconia based ceramics have been widely used for thermal barrier coatings (TBCs). When TBC is exposed to thermal cycling during real applications, the TBC may fail due to several mechanisms: (1) phase transformation into yttrium-rich and yttrium-depleted regions, When the yttrium-rich region produces pure zirconia domains that transform between monoclinic and tetragonal phases upon thermal cycling; and (2) cracking of the coating due to stress induced by erosion. The mechanism of erosion involves gross plastic damage within the TBC, often leading to ceramic loss and/or cracks down to the bond coat. The damage mechanisms are related to service parameters, including TBC material properties, temperature, velocity, particle size, and impact angle.

The goal of this thesis is to understand the structural and mechanical properties of the thermal barrier coating material, thus increasing the service lifetime of gas turbine engines. To this end, it is critical to study the fundamental properties and potential failure mechanisms of zirconia. This thesis is focused on investigating the structural and mechanical properties of zirconia. There are mainly two parts studied in this paper, (1) ab initio calculations of thermodynamic properties of both monoclinic and tetragonal phase zirconia, and monoclinic-to-tetragonal phase transformation, and (2) image-based finite element simulation of the indentation process of yttria-stabilized zirconia.

In the first part of this study, the structural properties, including lattice parameter, band structure, density of state, as well as elastic constants for both monoclinic and tetragonal zirconia have been computed. The pressure-dependent phase transition between tetragonal (t-ZrO2) and cubic zirconia (c-ZrO2) has been calculated using the density function theory (DFT) method. Phase transformation is defined by the band structure and tetragonal distortion changes. The results predict a transition from a monoclinic structure to a fluorite-type cubic structure at the pressure of 37 GPa. Thermodynamic property calculations of monoclinic zirconia (m-ZrO2) were also carried out. Temperature-dependent heat capacity, entropy, free energy, Debye temperature of monoclinic zirconia, from 0 to 1000 K, were computed, and they compared well with those reported in the literature. Moreover, the atomistic simulations correctly predicted the phase transitions of m-ZrO2 under compressive pressures ranging from 0 to 70 GPa. The phase transition pressures of monoclinic to orthorhombic I (3 GPa), orthorhombic I to orthorhombic II (8 GPa), orthorhombic II to tetragonal (37 GPa), and stable tetragonal phases (37-60 GPa) are in excellent agreement with experimental data. In the second part of this study, the mechanical response of yttria-stabilized zirconia under Rockwell superficial indentation was studied. The microstructure image based finite element method was used to validate the model using a composite cermet material. Then, the finite element model of Rockwell indentation of yttria-stabilized zirconia was developed, and the result was compared with experimental hardness data.

Key words: zirconia; thermal barrier coating; indentation; first principles; finite element

1. INTRODUCTION

1.1 Background

Thermal barrier coatings (TBCs) are refractory-oxide ceramic thin films coated to the surfaces of metal or alloy parts in the hot region of modern gas-turbine engines, enabling the engines to operate at high gas temperatures (see Figure 1.1). Gas-turbine engines are Carnot engines which can be used to power aircrafts and to generate electricity. Temperature is directly related to the efficiency of the gas turbine engines [1].

As one can see in Figure 1.2, thermal barrier coatings consist of the oxide ceramic coating (topcoat), and the superalloy engine part beneath it (substrate), and also two other layers in between. These two layers include a metallic layer (bond coat) that is more oxidation-resistant than the superalloy, and a very thin, thermally grown oxide (TGO) layer that forms between the bond coat and the top coat as a result of bond-coat oxidation in-service. Due to the composition, the bond coat can form a TGO made of -Al_2O_3, a mechanically robust, effective barrier to oxygen diffusion [1]. In current engines, the ideal power output increases with the gas temperature at the turbine inlet, but as the gas temperature rises, so does the work required to provide the flow of cooling air needed to bring the hot section materials to within their temperature limitations. The gap between ideal and actual power output represents an inefficiency whose root cause is the inability of component materials to withstand higher engine temperatures [2]. TBCs help close this gap by sustaining a temperature gradient between the hot gas stream and the component surface, typically lowering the maximum surface temperature of the component by 200 ^{o}C. The lower surface temperature allows the engine designer to either reduce the cooling air to raise effi-

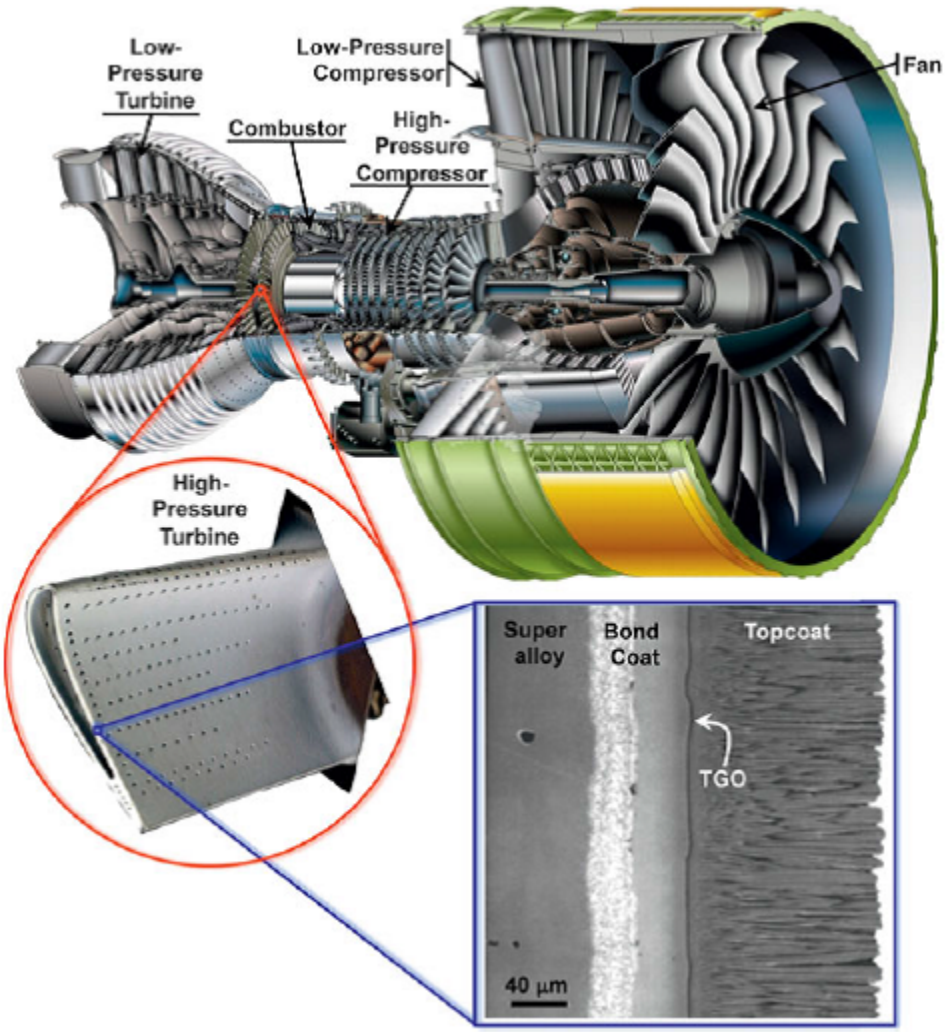

Figure 1.1. Application of thermal barrier coating on gas turbine engines [1]

ciency and save fuel, increase the turbine inlet temperature and increase power, or retain the same flow of cooling air and improve component durability.

Modern thermal barrier coatings have their origins in the 1970s. Flame-sprayed ceramic coatings, such as alumina, zirconia-calcia, or zirconia-magnesia, were developed as an alternative to frit enamels, which were applied to aerospace applications in the 1950s, and used in relatively undemanding roles [3,4]. Plasma spraying of materials, which was developed as an offshoot of research into low thrust plasma arc engines for spacecraft, proved to be an efficient and effective way of depositing ceramics. By

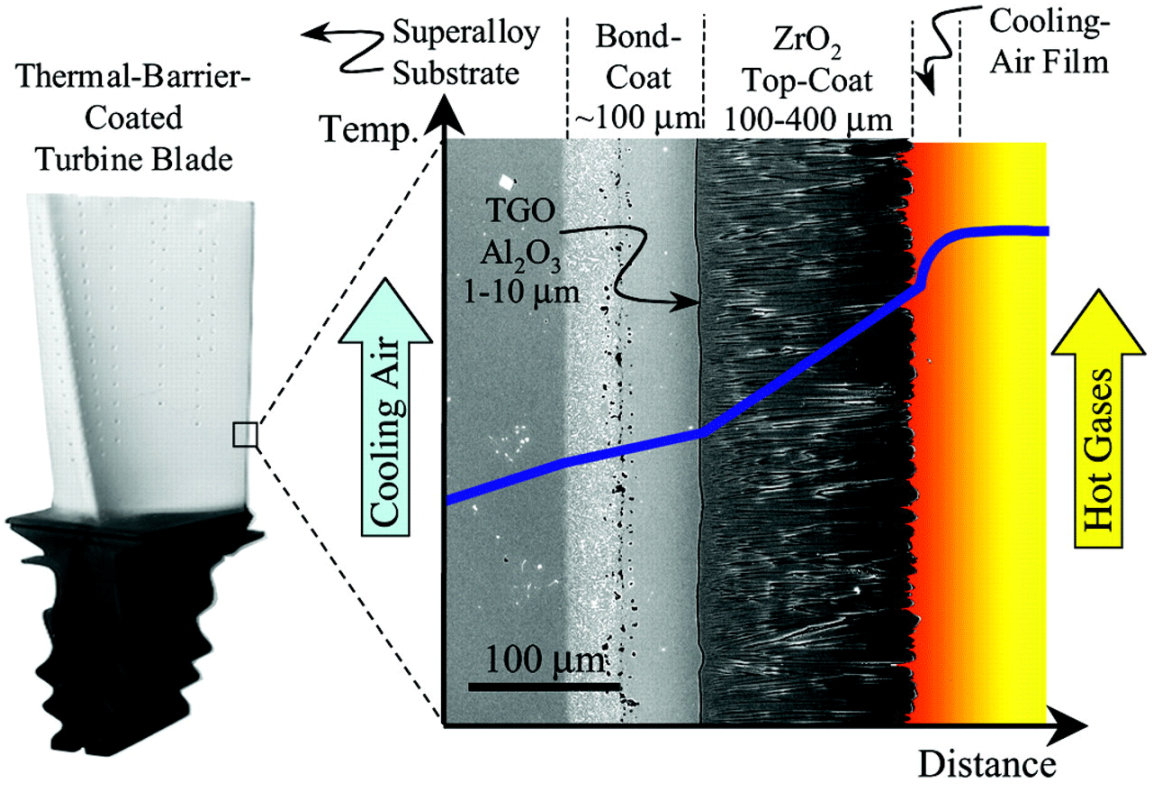

Figure 1.2. Layered structure of thermal barrier coatings

1970, plasma-sprayed ceramics began to be used in low risk hot-sections of aircraft engines. As TBCs achieved more advanced applications and hotter temperatures, around 1978, materials researchers found that 6-8% yttria-stabilized zirconia, which is still used today, optimized the durability of coatings in typical operation [3, 5]. TBCs have advanced from use in low risk areas of the engine to the more demanding hot-sections due to the confidence gained by advances in life prediction along with material improvements,. Life prediction methods, initiated by NASA in the early 1980s [3, 4], have advanced significantly up to the present, but the lack of a robust and physically-based life prediction method persists, and precludes TBCs from being used to the fullest extent that the current materials allow.

The temperature of the hot gas in the combustor and at the turbine inlet is typically much hotter than the melting temperature of the superalloy components, which is usually around 1300 ^{o}C. In service, the engine either cycles frequently, as in the case of airplane engines, cooling and heating of the TBC rapidly for many cycles, or it cycles infrequently but for long durations, as in the case of base-load power generating turbines. In these extreme environments, a TBC is susceptible to an array of structural and material phenomena that lead to the eventual degradation and failure of the TBC, exposing the underlying metal to dangerous gases which can accelerate the failure of the component. Because of the apprehension about premature failure with little warning, TBC systems in practice are not designed to their full potential, leaving increases in efficiency and performance on the table. The reason for the apprehension lies in the fact that although TBCs are over 30 years old, they are still not well understood [6]. The high temperature interplay between mechanical and material phenomena like thermal expansion, diffusion, oxidation, creep, microCracking, sintering, and fatigue is difficult to untangle and leads to very complex and sensitive stress states, making life prediction difficult. Thus, the study on thermal barrier coating materials is important.

1.2 Reviews of Thermal Barrier Coatings

TBC systems are composed of four layers (Figure 1.2): (1) a ceramic top coat, typically yittria-stabilized zirconia (YSZ); (2) a thin layer of thermally grown oxide (TGO) that forms during service; (3) an intermetallic bond coat (BC), typically MCrAlY or an aluminide; and (4) the substrate, or underlying component, which in the hot sections of an engine is usually a Ni-based superalloy. These four layers comprise a TBC system. In discussion, however, TBC is sometimes meant to refer only to the YSZ top coat.

The function of the top coat is to provide a temperature drop across its thickness, insulating the substrate from the hot gas stream. Only materials with very low thermal conductivities can achieve this while maintaining a minimal thickness, precluding most metals. A high melting temperature is also required, so ceramics emerge as the obvious choice. The thermal expansion coefficient is also very important, as the ceramic must be able to somewhat keep up with the metal layers as they expand and contract. Low stiffness is required as well, so that the ceramic can absorb any strain imposed upon it by thermal mismatch. Other desirable material properties include phase stability to avoid large strains due to transformation, a low density to promote strain tolerance and reduce weight, and a high hardness to resist erosion and foreign body impact.

The material that is most widely chosen in industry to meet these criteria is zirconia (ZrO_2) which has one of the lowest thermal conductivities of any ceramic materials. The conductivity is further reduced during deposition, owing to the resultant microstructure. Zirconia also has a preferable thermal expansion coefficient and a low stiffness due its particular microstructure. Zirconia in its pure form, however, undergoes a phase transformation from monoclinic tetragonal or cubic under different temperature ranges. These transformations are accompanied by large volume changes, which when constrained, as is the case with TBC applications, lead to very large stresses, likely resulting in failure.

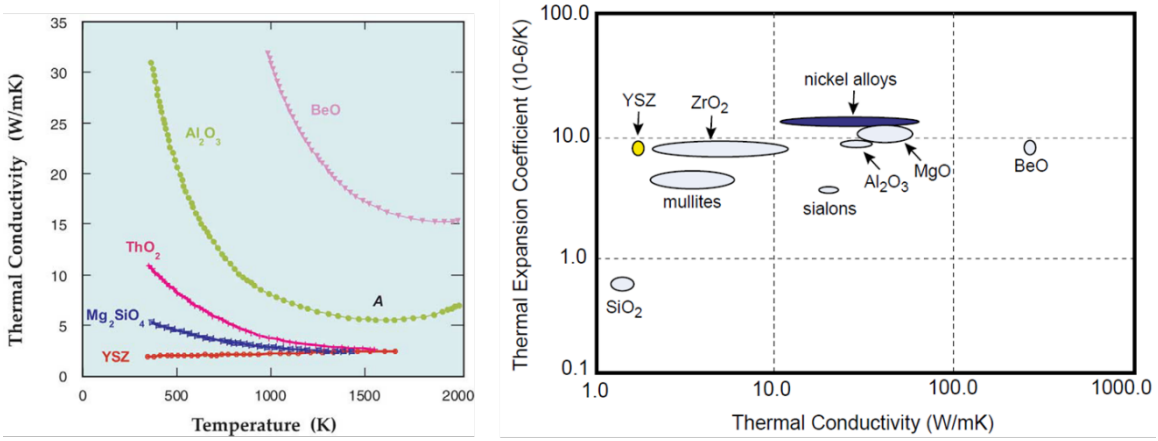

(a) (b)

Figure 1.3. (a) Thermal conductivity versus temperature for several refractory compounds. (b) Materials usually exhibiting low thermal conductivity [7]

Stabilizing the zirconia so that it reduces the severity of these transformations can be done by doping it with various oxides [8, 9]. Yttria has emerged as the ideal dopant because it prohibits the zirconia from transforming from the tetragonal to monoclinic phase, which is accompanied by a 4% volume reduction. The metastable tetragonal (t) phase of zirconia, which is formed on rapid cool down of the coating after doping with yttria, has the highest fracture toughness of any form of zirconia. The metastable t phase, however, can transform to the monoclinic phase under applied stress. Furthermore, if the zirconia is allowed to cool in a certain manner after forming, a non-transformable tetragonal (t) phase will form, which retains the high fracture toughness and will not transform under stress. The amount of t phase present is maximized with about 8 weight percent yttria, so the material used most often for deposition of the top coat in TBCs is either 7 or 8 wt. % t yttria-stabilized zirconia (7YSZ or 8YSZ).

1.3 Goal and Objectives

When TBC is exposed to thermal cycling during real applications, the TBC may fail due to several mechanisms: (1) phase transformation into yttrium-rich and yttrium-depleted regions, when the yttrium-rich region produces pure zirconia domains that transform between monoclinic and tetragonal phases upon thermal cycling; and (2) cracking of the coating due to stress induced by erosion. The mechanism of erosion involves gross plastic damage within the TBC, often leading to ceramic loss and/or cracks down to the bond coat. The damage mechanisms are related to service parameters, including TBC material properties, temperature, velocity, particle size, and impact angle.

The goal of this thesis is to study the structural and mechanical properties of the thermal barrier coating material, thus increasing the service lifetime of gas turbine engines. To this end, it is critical to understand the fundamental properties and potential failure mechanisms of zirconia. The specific objectives of this work are:

(1) ab initio calculations of thermodynamic properties of both monoclinic and tetragonal phase zirconia, and monoclinic-to-tetragonal phase transformation; and

(2) image-based finite element simulation of the indentation process of yttria-stabilized zirconia

Achieving the above objectives will help understand the mechanical behavior of thermal barrier coating materials, thus the failure mechanisms, and improve TBC performances.

1.4 Thesis Outline

This thesis will develop multiscale computational models to simulate the properties of zirconia for thermal barrier coating applications. Given the objectives outlined in Section 1.3, two types of computational models will be developed: (1) atomistic scale simulation using the first principles method, and (2) continuum scale modeling using the finite element method. Properties that affect the performance of thermal barrier coatings, such as thermodynamic properties and mechanical properties, will be studied.

In the first part of this study, the structural properties, including lattice parameter, band structure, density of state, as well as elastic constants for both monoClinic and tetragonal zirconia are computed. Pressure-dependent phase transition between tetragonal (t-ZrO_2) and cubic zirconia (c-ZrO_2) are calculated using the density function theory (DFT) method. Phase transformation is defined by the band structure and tetragonal distortion changes. Thermodynamic property calculations of monoclinic zirconia (m-ZrO_2) are also carried out. Temperature dependence of heat capacity, entropy, free energy, Debye temperature of monoclinic zirconia, from 0 to 1000 K, are computed and compared with those reported in literature. In the second part of this study, the mechanical response of yttria-stabilized zirconia under Rockwell superficial indentation is studied. The microstructure image based finite element method is used to validate the model using a composite cermet material. Then, the finite

element model of Rockwell indentation of yttria-stabilized zirconia is developed, and the result is compared with experimental hardness data.

The structure of the thesis is as follows. Chapter 1 provides an introduction to thermal barrier coatings. Structures of thermal barrier coating are illustrated. Several commonly used materials for thermal barrier coatings are mentioned and compared. Literature related to the TBC materials are also discussed in Chapter 1. In Chapter 2, the study is mainly focused on the atomistic simulation of pure zirconia, phase transition and thermal properties. Chapter 3 aims to develop a finite element model for yttria-stabilized zirconia Rockwell indentation using the image based method. The method is validated and then applied to the indentation modeling. Chapter 4 provides a summary and discussion of future work.

2. FIRST PRINCIPLES STUDY OF THERMAL AND STRUCTURAL PROPERTIES OF ZIRCONIA

2.1 Introduction

NiAl based aluminate was first commonly used for thermal barrier coating material. However, it was eliminated because of short fatigue life [7]. Several improvements have been made in recent years, and the state of the art commercially used material for thermal barrier coating is now yttria-stabilized zirconia (YSZ). YSZ has the following characteristics: high melting temperature of 2700 ^{o}C [10], low thermal conductivity of about 2.3 W/(^{o}C -m) at 1000 ^{o}C [6]and chemical stability [6].

2.1.1 Phases of Zirconia

Zirconia has polymorphic crystallographic structures [11]. Based on temperature, zirconia can exist in three phases: monoclinic, tetragonal and cubic phases [12] (See Figure 2.1). At room temperature, the structure of zirconia is monoclinic, and this structure will not change until 1170 ^oC. As temperature increases from 1170 ^oC to 2370 ^oC, the structure of zirconia changes to tetragonal, which is called the m-t phase transition. When temperature exceeds 2370 ^oC, cubic phase zirconia is formed [13].

An effective way to stabilize zirconia in tetragonal and cubic phase is doping. Commonly used dopants are oxides, such as magnesia (MgO) and yittria (Y_2O_3). Over a wide temperature range, stabilization of zirconia can be done by replacing Zr^{4+} ions using dopant ions that have a larger atomic size. The resulting doped zirconia materials are termed stabilized zirconia [14]. With these dopants in the structure, zirconia can maintain a metastable t phase from room temperature to about 1200 ^oC. At higher temperature, t phase YSZ changes to a composition of cubic and tetragonal phase structure [15]. Although the most well studied and commercialized material

for thermal barrier coatings is yttria-stabilized zirconia, in this study, for simplicity purpose, zirconia without any doping will be investigated and discussed.

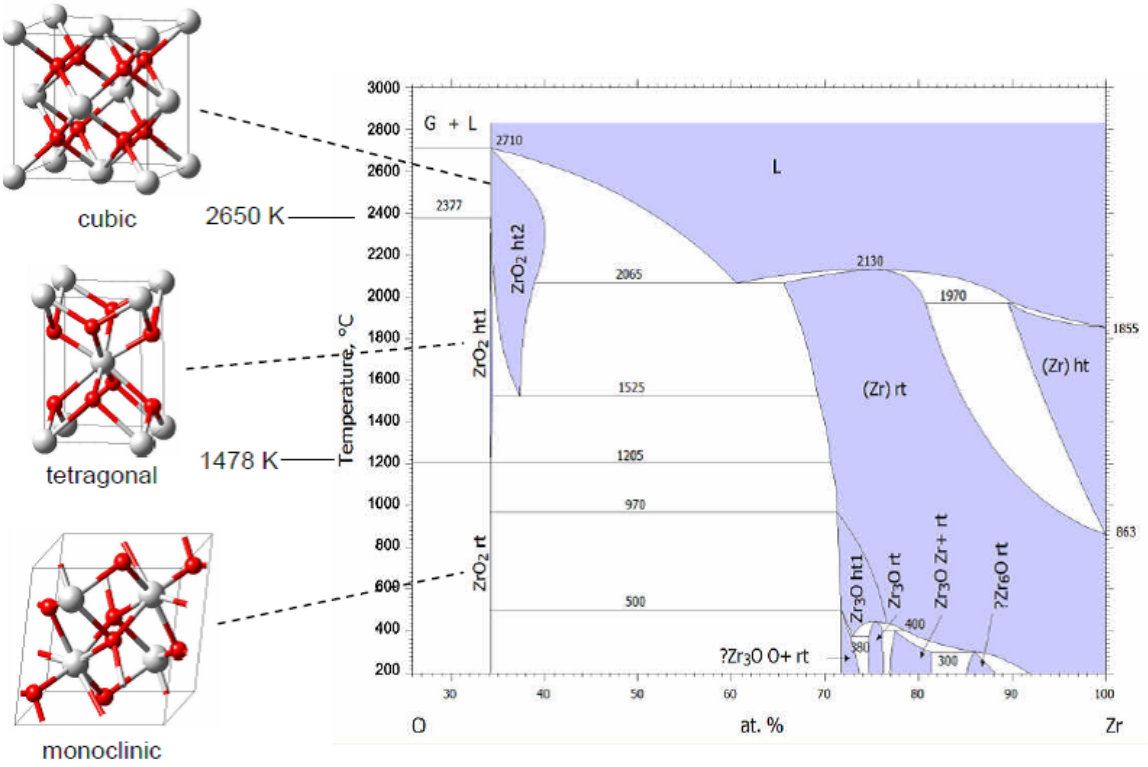

Figure 2.1. Zirconia phase diagram [16]

2.1.2 First Principles Simulation of Zirconia

Theoretical studies of zirconia, especially phase transition and thermodynamic properties of zirconia, have been developed for decades. For crystalline structured materials, density functional theory (DFT) is the well-established method for such first principles calculation. Many attempts are made to investigate the properties and the phase transition nature of zirconia [17, 18].

Study of the thermal properties of different phases of zirconia has been reported. Temperature-based phase transition of zirconia can be derived by those properties.

Tojo et al measured the specific heat capacity at constant volume experimentally [19]. They tested the thermal properties of pure zirconia and YSZ by adiabatic calorimetry measurement at temperatures between 13 K and 300 K. Lou et al [20] investigated the thermodynamic properties and temperature-based monoclinic to tetragonal phase transition for both ZrO_2 and HfO_2 using the ab initio method. They presented a method for both hafnia and zirconia, and the temperature dependency of heat capacity of two materials was validated.

Lattice dynamics is also one of the important aspects in such studies, because it has been suggested that soft phonon mode mechanism is the major cause of zirconia phase transformations [21]. One of the important issues is that the density functional theory calculation is performed in conditions where temperature is 0 K. However, at this temperature, most phases could not be stable without any external pressure or internal dopants. This issue increases the challenges when comparing DFT computational results with experimental results. Therefore, a study of pressure-dependent lattice dynamic study is necessary. Ozturk and Durandurdu [22] conducted a comprehensively theoretical study on high pressure-based phase transition of zirconia. Victor et al [23] used CASTEP code to develop an ab initio model of tetragonal zirconia with external pressure. They found that the lattice structure of t-ZrO_2 will change to cubic structure under the pressure of 37 GPa. Structural properties of zirconia, such as band structure and density of state, were also investigated by DFT calculations [17, 24]. The present study also emphasizes pressure dependency of tetragonal zirconia, and investigates the structural properties of t-ZrO_2 transformation under hydrostatic compressive pressures.

Pressure-dependent phase transition of m-ZrO_2 is another aspect of interest in the phase transition studies. Figure 2.2 shows the temperature, pressure phase diagram [25]. Pure zirconia maintains monoclinic structure at ambient pressure. Three high pressure phases of zirconia have been reported by experimental tests, orthorhombic I, orthorhombic II, and a tetragonal phase which is different from the high temperature tetragonal at ambient pressure. Monoclinic to orthorhombic phase transition happens

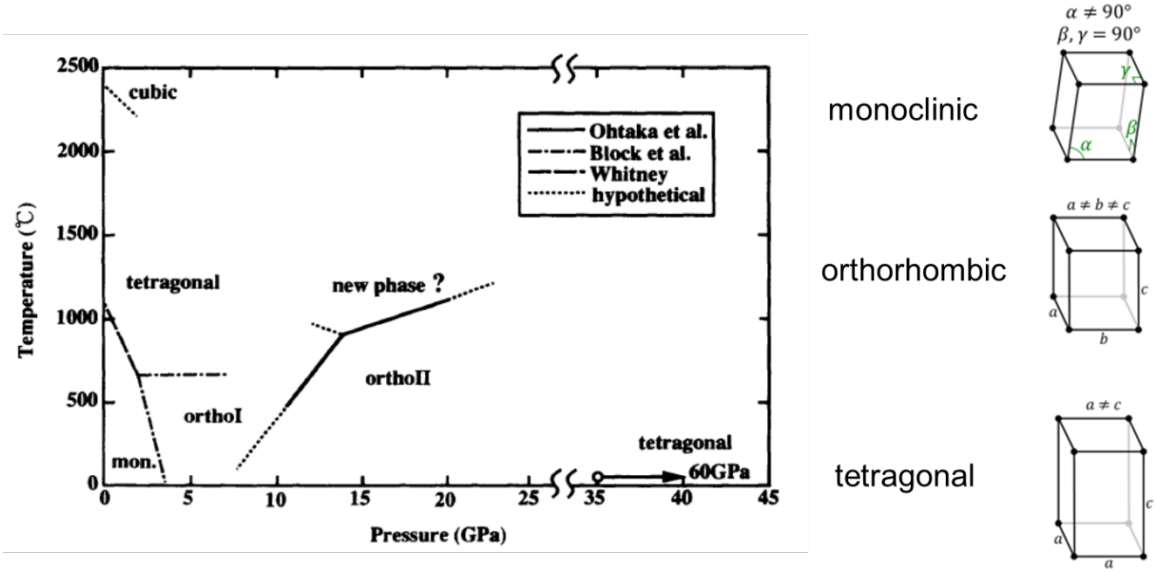

Figure 2.2. Phases of zirconia at different temperature and pressure [25]

at the compressive pressure of 3 GPa at room temperature [26]. By doing nucleation and growth processing, the orthorhombic I to orthorhombic II phase transformation was accomplished by Ohtaka et al [27]. Arash et al reported the orthorhombic I to tetragonal phase transition pressure of 37 GPa at room temperature [28]. This phase maintains stablility until 60 GPa [25]. Several simulations on atomistic scale were tried to predict the phase transition pressure for m-ZrO_2: an ab initio study on phase transition of zirconia at high pressure was reported by ztrk et al [29]. Their simulation results, however, have much higher values for phase transition pressure than the experimental data from other studies. In this study, the CASTEP model was developed in order to develop a compatible ab initio model for high pressure phase transition of m-ZrO_2.

The structure of this chapter is described as follows. Section 2 describes the calculation details. Algorithms, cutoff energy settings, k-points settings, convergence criteria, lattice definitions are presented in this section. In section 3, computational

results, following the order of thermal and phase transition, are presented and then compared with the related data in literature.

2.2 Calculation Methods

2.2.1 Thermodynamic Properties of m-ZrO_2

Thermal properties were calculated using the first principles methods. First principle theory is also called ab initio theory. It calculates material behaviours without any definition of material properties. The calculation is based on Schrödinger's equation with appropriate assumptions. Calculations of thermal properties are conducted using two ab initio software packages [12, 30–32].

All the calculations were based on the density functional theory (DFT) [33,34]. In this theory, all calculations are conducted in ground state (temperature is 0 Kelvin). The total energy of the ground state is uniquely determined by the electron density:

$$E = E[n(r)] \tag{2.1}$$

where E: total energy of the ground state; n: electron density; r: position of electrons. The main purpose of ab initio calculation is to solve the Schrdinger equation (Eq. (2.1)). Methods used are numerous. In general, two theories are used: density functional theory (DFT) and Hartree-Fock (HF). Comparing the algorithms of these two methods, DFT solves the Kohn-Sham equation, whereas the HF method solves Roothaan equations. Most calculations use either one of two methods. However, some calculations use combined methods, which is called the hybrid functional approach. Due to the complexity of solving Eq.(2.1), Kohn-Sham equations [33] (equations (2.2) and (2.3)) are actually adopted to solve the governing equation which has some assumptions such as local density approximation (LDA), generalized gradient approximation (GGA) and the hybrid of these two assumptions.

$$\left(-\frac{\hbar^2}{2m}\nabla^2 + v_{ext}(r) + v^e_{coul}(r) + v_{xc}(r)\right)\psi nk(r) = \varepsilon_{nk}\psi_{nk}(r) \tag{2.2}$$

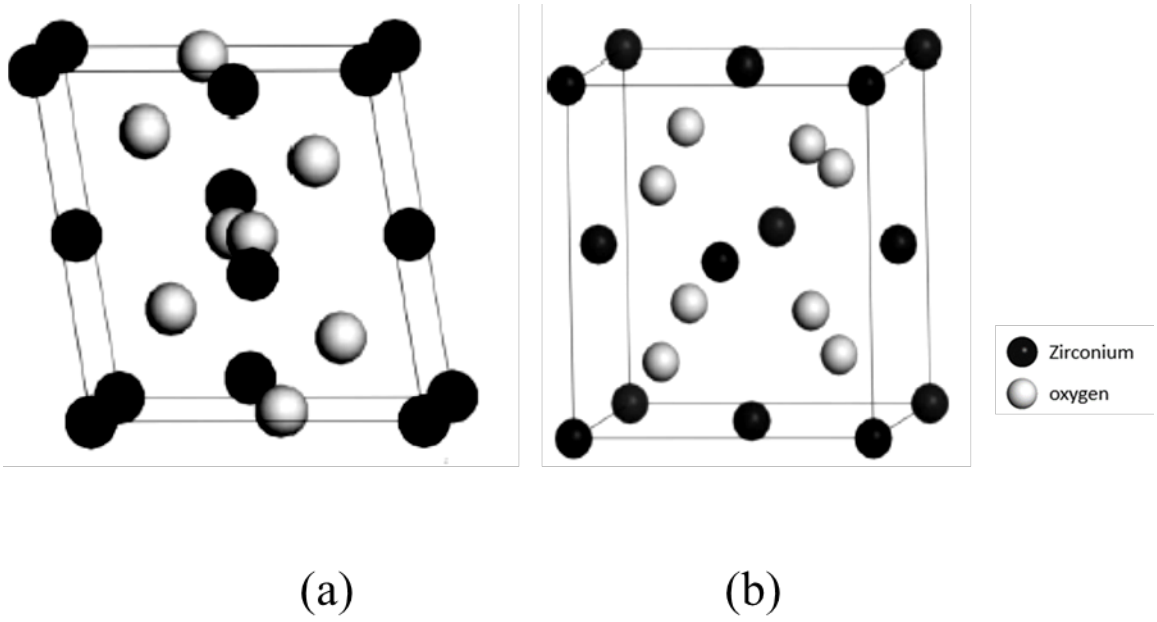

Figure 2.3. (a) Unit cell of m-ZrO_2.(b) Unit cell of t-ZrO_2 [20]

$$n(r) = \sum_{nk}^{\#of\_e} |\psi_{nk}(r)|^2 \tag{2.3}$$

where r is the distance between two electrons, equation (2.2) represents the interaction between two electrons, to solve equation (2.1), the ab initio sum up all interactions (shown in equation (2.3)) and plug into equation (2.1), so that the total energy at ground state can be solved.

The crystal structure of zirconia is illustrated in Fig. 2.3. Monoclinic zirconia structure is shown in Fig. 2.3 (a), bond angles of this structure include two 90 degrees and one 100 degrees [34]. Lattice parameters of both monoclinic and tetragonal structures are defined according to databases [34,35] and then relaxed using *ab initio* method.

Calculations were conducted at GGA+PBE with a unit cell of 2 formula units (2 Zr and 4 O) using CASTEP code in the Material Studio modelling package (MS). The convergence criteria of the free energy with the k-points sampling and the cut-

off energy for approximation was cautiously examined. In order to make sure that the calculation is converged, the total energy difference was set below 10^{-5} eV. The Monkhorst-Pack defined $3 \times 3 \times 1$ k-points was applied for the unit cell mesh based on Brillouin zone integration. For the plane waves, cut-off energy was set to be 800 eV. Before the thermodynamic calculation, an energy minimization study was conducted, so that the lattice parameter and the ion positions were optimized and the unit cell was relaxed without any pre-stress. After the optimization of structure, a phonon calculation was performed to investigate the thermal properties of monoclinic zirconia based on the Debye theory.

Monoclinic phased zirconia (m-ZrO_2) thermodynamic property calculations were also carried out using the Vienna *ab initio* Simulation Package VASP [30,32] coupled with PHONOPY [36]. In order to reach the energy convergence of 10^{-6} eV, the cutoff energy was set to 600 eV. The Brillouin zone integration was defined as Monkhorst-Pack mesh with k points of $5 \times 4 \times 3$ grid. Superposition was generated by Phonopy after the geometry optimization. Specific heat capacity at constant volume (C_v) was calculated using the following equation [31]:

$$Cv(T) = \frac{1}{4k_B T^2} \int_0^\infty d\omega g(\omega) \frac{\hbar^2 \omega^2}{\sinh^2\left(\frac{\hbar\omega}{2k_B T}\right)} \tag{2.4}$$

where T is temperature, k_B is the Boltzmann constant, ω is phonon frequency, $\hbar$ is the Planck constant.

Density of state, temperature dependence of free energy, constant volume specific heat capacity were calculated and compared with experimental or others simulation results [19, 20].

2.2.2 Phase Transition Simulation of Zirconia

This work investigates the structural properties of both tetragonal phase zirconia (t-ZrO_2) and monoclinic zirconia (m-ZrO_2) under compressive pressures. For compressed t-ZrO_2, according to soft mode mechanism [37], tetragonal distortion occurs

when a hydrostatic compression is applied. As the tetragonal distortion increases, t-ZrO_2 will transform to a cubic structure (c-ZrO_2). For m-ZrO_2, when external pressure is applied, there will be a series of phase transition with the increasing of pressure according to experiment observations. The basic sequence is monoclinic to orthorhombic I, orthorhombic I to orthorhombic II, and orthorhombic II to tetragonal, and the specific transition pressure value will be determined by this calculation.

In the present calculations, the energy cutoff for expanding wave functions was set to 750 eV. For the Brillouin zone integration, Monkhorst Pack of $8 \times 8 \times 6$ k-points mesh was applied. Convergence criterion was set to 1×10^{-8} eV/atom. A convergence study based on different k-point settings was conducted. Comparing k-point of $8 \times 8 \times 6$ to k-point of $5 \times 5 \times 3$ was done by previous work [17,18,21,38,39].

The lattice structure of t-ZrO_2 is shown in figure 7, a, b, and c is the lengh from origin to the points illustrated in this figure. One factor that defines the structure of tetragonal crystal is the tetragonal distortion factor, A:

$$A = \frac{c}{a\sqrt{2}} \tag{2.5}$$

where a and c are the lattice parameters. For a prefect cubic structure, A = 1, so that A-1 = 0. One of the objectives in this paper is to measure the tetragonal distortion factor of the compressed t-ZrO_2.

2.3 Results and Discussion

2.3.1 Thermodynamic Properties

Thermodynamic properties of zirconia were carried out by both VASP and Material Studio simulation packages. At the beginning, in order to get accurate calculation results, a geometry optimization was cautiously conducted. Material Studio CASTEP module calculated the lattice parameters based on energy minimization. Debye temperature, temperature dependence of entropy, enthalpy, free energy and specific heat capacity under constant volume were also determined.

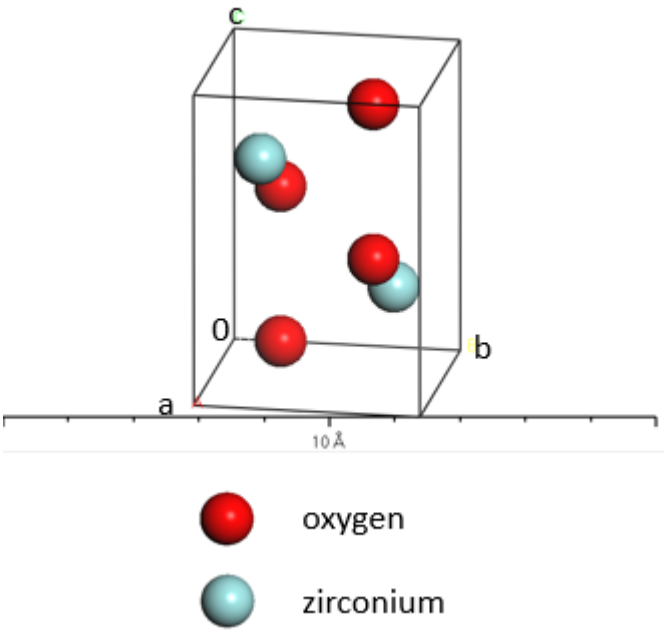

Figure 2.4. Crystal structure of t-ZrO_2

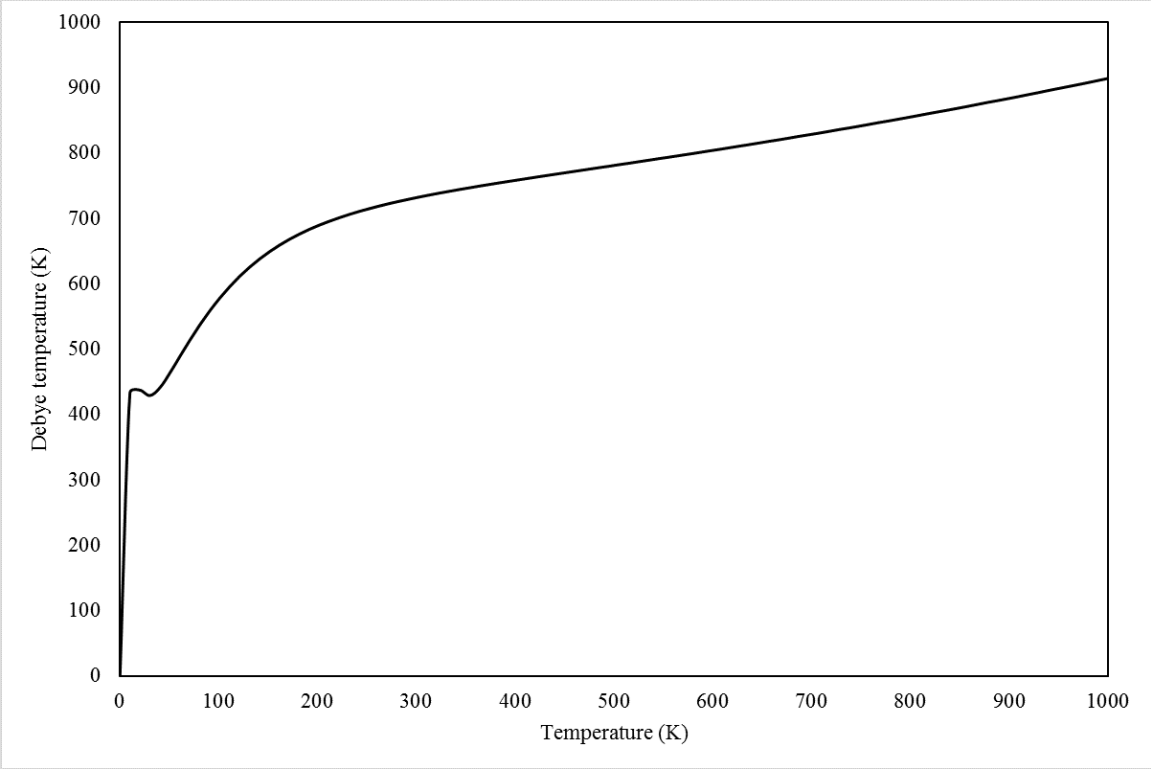

Figure 2.5. Debye temperature of m-ZrO_2 from 0 to 1000K

Debye temperature from 0 to 1000 K of m-ZrO_2 was obtained (See figure 2.5). During phonon vibration, the highest mode of vibration of crystal can be presented by the Debye temperature. With this data, specific heat at a constant volume can be obtained by differentiation with respect to temperature.

With the Debye temperature, the thermodynamic properties of m-ZrO_2 were achieved. Figure 2.6(a) shows the enthalpy, entropy, free energy and heat capacity at temperature from 0 to 1000K. Figure 2.6(b) shows the comparison of these results with others.

Figure 2.7 shows temperature dependence (from 0 to 350K) of specific heat capacity at constant volume of m-ZrO_2 compared with both experimental [19] and simulation [20] results, respectively. As seen in the figure, the agreement with the experimental data is excellent.

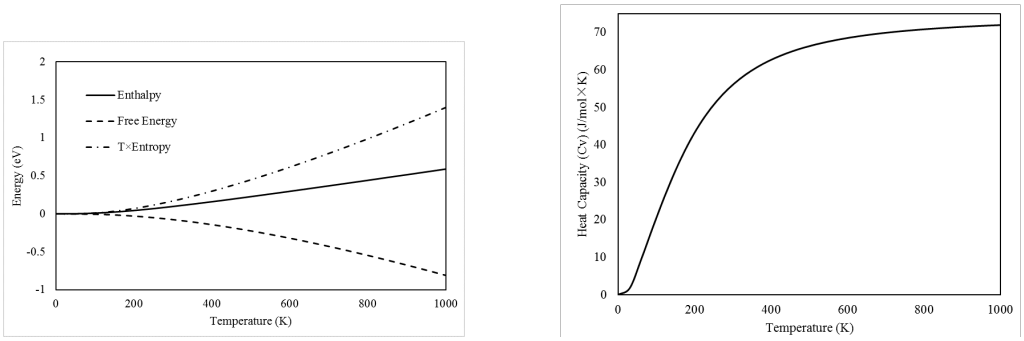

Figure 2.6. Thermodynamic properties of m-ZrO_2 from 0 to 1000 K; (a) enthalpy, entropy and free energy; (b) specific heat capacity

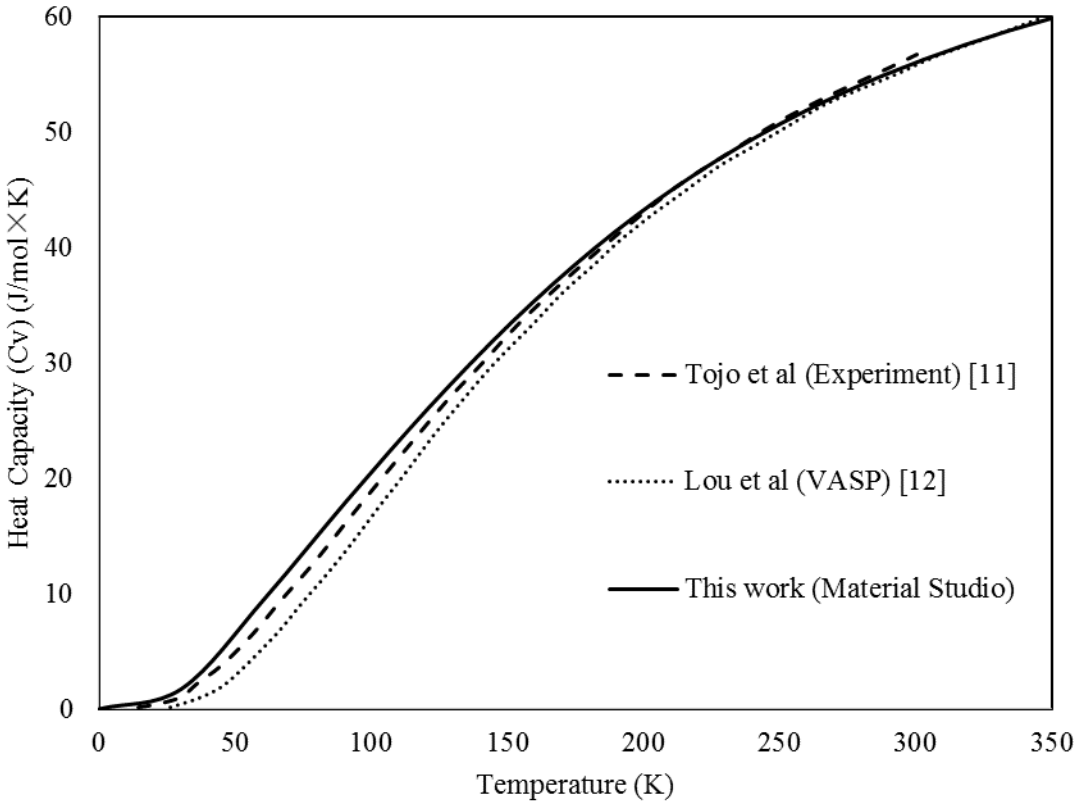

Figure 2.7. Heat capacity at constant volume of m-ZrO_2

Lattice relaxation was the first step of VASP calculations. Figure 2.8 shows the calculated free energy of different lattice parameters. VASP calculates the free energy for a monoclinic crystal structure with a specific lattice parameter. In this figure,

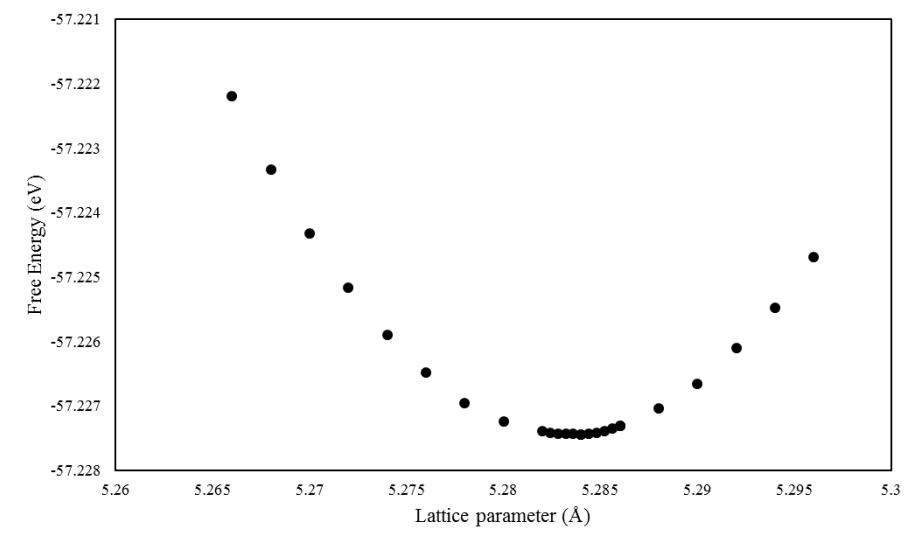

Figure 2.8. Lattice parameter versus free energy of m-ZrO_2

from 5.26 $\overset{0}{A}$ to 5.30 $\overset{0}{A}$, the energy curve had the lowest point of about -57.2 eV, corresponding to the lattice parameter of 5.284 $\overset{0}{A}$. The parameter with the lowest energy represents that crystal at this lattice parameter is the most stable, which means that this structure has no pre-stress. In other words, it was relaxed at 5.284 $\overset{0}{A}$. After relaxation of the monoclinic zirconia unit cell, optimized lattice parameter was achieved and compared with similar studies. The comparison of lattice parameter is shown in Table 2.1.

Table 2.1. Original and optimized lattice constants and comparison

Lattice parameter	**Before relaxation [34]**	**VASP Relaxed**	**MS relaxed**	**In literature [20]**
a ($\overset{0}{A}$)	5.1496	5.1257	5.175347	5.115
b ($\overset{0}{A}$)	5.2076	5.1723	5.241449	5.230
c ($\overset{0}{A}$)	5.3163	5.2844	5.358938	5.260

Based on the optimized crystal structure, 18 superpositions were generated using PHONOPY, and the thermal properties were calculated. Figure 2.9 (a) shows the results for the monoclinic phase including entropy, enthalpy, free energy change with temperature from 0 to 1000K, whereas Figure 2.9 (b) shows temperature dependence of specific heat capacity at constant volume done by this work, as well as the comparison with both experimental [19] and simulation [20] results. The result from CASTEP calculation was included. As seen in Figure 2.9 (b), the comparison shows an excellent agreement.

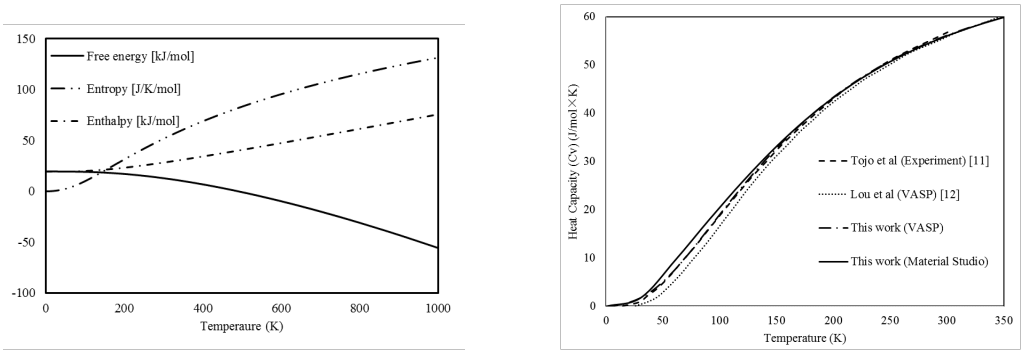

Figure 2.9. (a)m-ZrO_2 entropy, enthalpy, free energy change according to temperature from 0 to 1000K; (b) temperature dependence of specific heat capacity at constant volume

2.3.2 Pressure Dependent Phase Transitions

As mentioned in section 2, increasing hydrostatic compressive pressure, the crystal structure of tetragonal zirconia has a tendency to transform to cubic structure. When the pressure reaches the critical value (phase transition pressure), phase transition from tetragonal to cubic occurs. Before the hydrostatic pressure is applied, accurate lattice parameters were calculated and compared with relative works, which are listed in Table 2.2.

Table 2.2. Comparison of t-ZrO_2 lattice parameters

Lattice parameter	**Before relaxation [35]**	**MS relaxed**	**In literature [16]**
a ($\overset{0}{A}$)	3.512	3.565265	3.5742
b ($\overset{0}{A}$)	3.512	3.565265	3.5742
c ($\overset{0}{A}$)	4.988	5.127827	5.1540

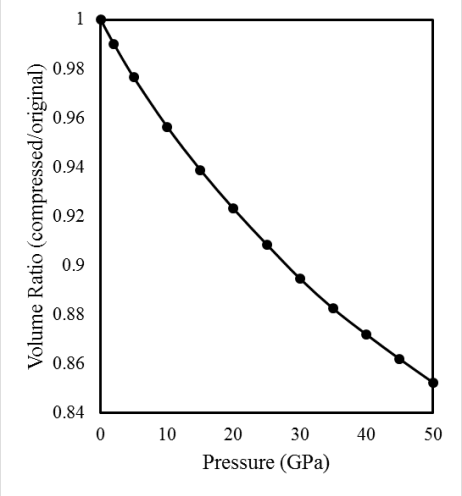

Figure 2.10. Crystal volume ratio change with increasing hydrostatic pressure

The relaxed crystal structure, volume change during the increasing of hydrostatic pressure, band structure change and lattice constant under pressure, were calculated.

Volume ratio is the compressed volume divided by the original crystal cell volume. As shown in figure 2.10, at the initial state, when no pressure was applied, the volume ratio was 1, since the volume did not change. With the increasing of compressive pressure, the volume ratio decreased gradually from 1 to 0.85, since the crystal cell shrank under compression.

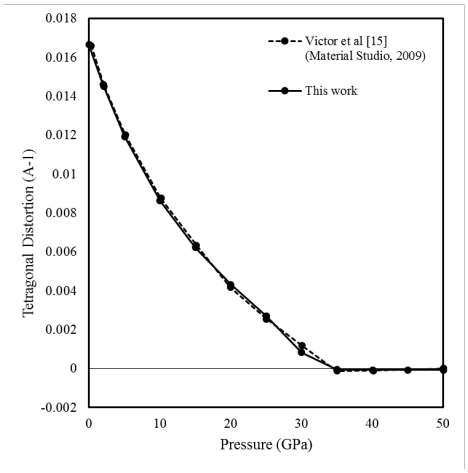

Figure 2.11. Tetragonal distortion change with increasing hydrostatic pressure

As discussed in section 2.2, the tetragonal distortion factor A, represents the tetragonal degree of a crystal. For example, a cell with A>1 means that this crystal has a tetragonal structure, and cubic structures have tetragonal distortion factor A=1. In Figure 2.11, the initial tetragonal distortion factor was about 0.017, which means the original structure of this cell was tetragonal, since no compression was applied. As the pressure increased, the tetragonal distortion (A-1) decreased from 0.017 at 0 GPa to 0 at about 37 GPa. This shows the intermediate states when the tetragonal phase was converting to cubic phase, since A was getting closer to 1. After the pressure reached 37 GPa, the tetragonal distortion factor A kept constant at 1. This means that after 37 GPa, the cubic structure is a stable phase.

Figure 2.12 shows the indirect band gap decreased during compression, band gap slope changed from 6.3 meV GPa^{-1} to 5.2 meV GPa^{-1} at the pressure of 37 GPa, indicating a phase transition from tetragonal to cubic phase.

Lattice constants were studied for the pressure dependence of m-ZrO_2, and the change of length of lattice parameters a, b and c (which can be seen in figure 2.13) were analyzed and plotted in Figure 2.14.

An ideal way to elucidate the mechanism of this phase change is to investigate directly the pressure dependence of the simulation cell vectors. Figure 2.14 shows the

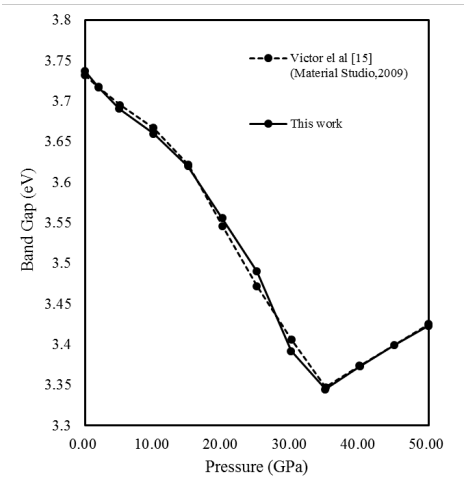

Figure 2.12. Indirect band gap change with increasing hydrostatic pressure

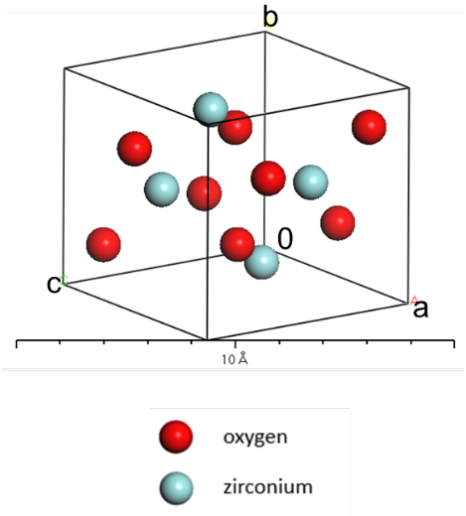

Figure 2.13. Crystal structure of m-ZrO_2

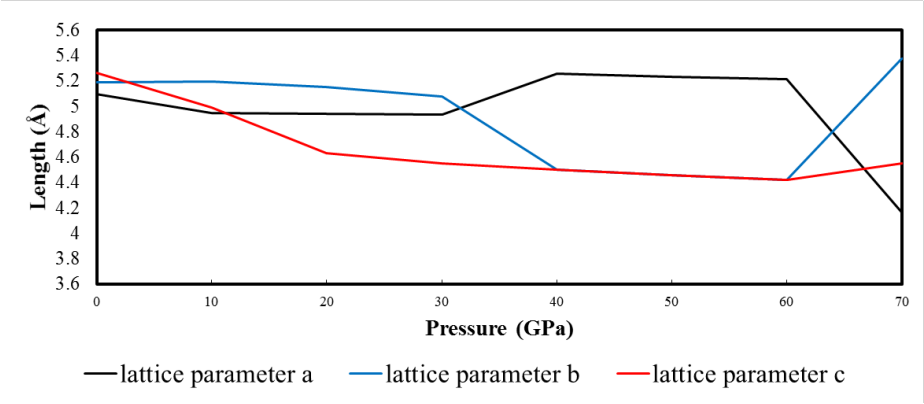

Figure 2.14. Calculated lattice parameters in the simulation cell

cell lengths and angles as functions of the applied pressure. As one can clearly see, the ZrO_2 structure exhibited a strong anisotropic compression. The c axis was found to be more compressible than the other axes. At about 3 GPa, the length of c became smaller than b, which indicates the monoclinic structure changed to orthorhombic I phase. After 10 GPa, it showed a change in slope and the compression in this direction becomes slower. That indicates the structure of ZrO_2 started to change to orthorhombic I [29]. When the pressure reached 40 GPa, the length of c and b were equal, which means the structure of zirconia is tetragonal. Also as can be seen in this figure, a and c kept equal until the pressure reached 60 GPa; this indicates the tetragonal structure is no longer stable at pressure higher than 60 GPa. These phase transition pressures agree well with the experimental phase transition pressures at 0 K in figure 2.2. The comparison of this work and the data read from figure 2.2 is shown in table 2.3.

Table 2.3. Comparison of calculated m-ZrO_2 phase transition pressures with experimental data

Phase transition	**Experiment**	**This work**
m-*ortho*I	3GPa	3GPa
*ortho*I-*ortho*II	8GPa	10GPa
*otrho*II-t	35GPa	37GPa
t phase	40GPa	60GPa

2.4 Summary

In this study, we present a series of atomistic simulations of zirconia, including monoclinic and tetragonal phases, using the first principles theory. Heat capacity at constant volume of m-ZrO_2 was calculated and found to be highly compatible with both experimental and others simulation results. Hydrostatic compression from 0 to

50 GPa was applied to the tetragonal zirconia. The results strongly supported that the tetragonal distortion disappeared at 37 GPa, and the structure of zirconia turns into cubic type. The tetragonal distortion kept decreasing under compression, until phase transition occurred. There was no further structure change after transition pressure. Tetragonal distortion factor kept constant at 1. The atomistic simulations correctly predicted the phase transitions of m-ZrO_2 under compressive pressures ranging from 0 to 70 GPa. The phase transition pressures of monoclinic to orthorhombic I (3 GPa), orthorhombic I to orthorhombic II (8 GPa), orthorhombic II to tetragonal (37 GPa), and stable tetragonal phase (37-60 GPa) are in excellent agreement with experimental data.

3. STUDY ON ROCKWELL INDENTATION OF YTTRIA-STABILIZED ZIRCONIA THERMAL BARRIER COATINGS

3.1 Introduction

Plasma sprayed yttria-stabilized zirconia coatings are being increasingly used as thermal barrier coatings for gas turbines and diesel engines [40]. Effective TBCs should exhibit low thermal conductivity, strong adherence to the substrate, and phase stability.

As mentioned in Chapter.1, erosion of thermal barrier coatings during operation is one of the difficulties, since it can cause failure and reduce fatigue life of TBC. As figure figure 3.1 shows, compared with other spray methods and bulk ceramic, the air plasma sprayed coatings have the highest erosion rate, which means that APS coating fails more easily due to erosion than other methods shown in this figure.

One thing that highly effects erosion is hardness of the coating, which can be measured by doing the indentation test. In a Rockwell indentation test, a diamond conical indenter with 200μm tip is applied on the surface of the pre-treated coating, and then the indenter moves toward the coating, which is called loading, followed by the release of the indenter, which is called unloading. By doing this process, the indenter mark and the indentation depth under a pre-defined load will be achieved, so that the hardness of the sample can be calculated.

The Rockwell hardness test consists of two major categories: the Regular Rockwell indentation test and the Rockwell Superficial indentation test. For thermal barrier coating as thin films, the Rockwell superficial test is applied. For the superficial Rockwell testing, all the minor loads are 3 kgf regardless of major loads. The major load can be different, usually chosen from 15 kgf, 30 kgf, or 45 kgf. Different scales

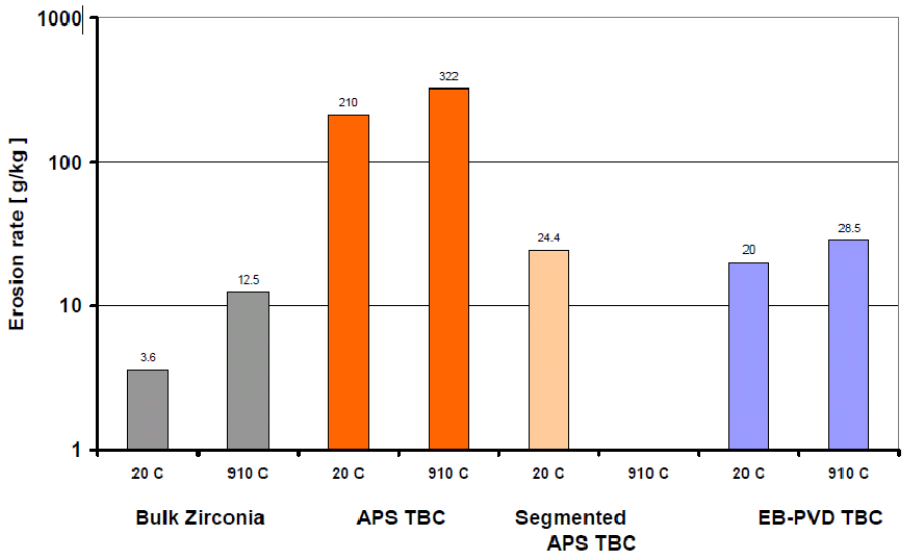

Figure 3.1. Comparison of the erosion performance of air plasma sprayed, EB-PVD and segmented plasma sprayed coatings at RT and 910°C. Data for bulk 7-YSZ is included as a reference [41]

are defined according to the combination of different major load and indenter shape (Table 3.1). In this study, the indentation test uses 15N scale.

Table 3.1. Superficial Rockwell scales

Scale Symbol	**Penetrator**	**Loda Force (kg)**
15 N	N Brale	15
30 N	N Brale	30
45 N	N Brale	45
15 T	$\frac{1}{16}$ in Ball	15
30 T	$\frac{1}{16}$ in Ball	30
45 T	$\frac{1}{16}$ in Ball	45
15 W	$\frac{1}{8}$ in Ball	15
30 W	$\frac{1}{8}$ in Ball	30
45 W	$\frac{1}{8}$ in Ball	45
15 X	$\frac{1}{4}$ in Ball	15
30 X	$\frac{1}{4}$ in Ball	30
45 X	$\frac{1}{4}$ in Ball	45
15 Y	$\frac{1}{2}$ in Ball	15
30 Y	$\frac{1}{2}$ in Ball	30
45 Y	$\frac{1}{2}$ in Ball	45

The indenter is pressed into the test sample under a minor load F_0 (Fig 3.2A) 3 kgf. As the equilibrium has been reached, the indicating device that follows the position of the indenter and so responds to changes in depth of indenter movement is set to a datum position. With the minor force is still applied, the major load force is applied additional to the minor load, which results the increase in penetration (Fig 3.2B). As the equilibrium has been reached again, the major load is removed while the minor load is still kept. There is a partial recovery of the indenter depth due

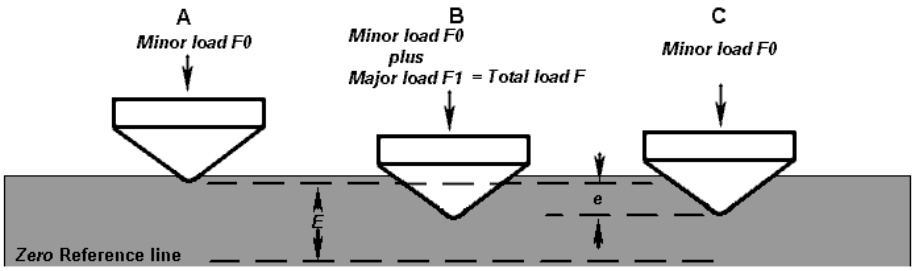

Figure 3.2. Principle of Rockwell indentation

to the spring back effect of the sample. The overall increase in depth of indenter, e, is used to calculate the number of Rockwell Superficial hardness using the following equation.

HR=E-e

(3.1)

where F_0 is the minor load(kgf), F_1 is the major load additional to the minor load (kgf), F is total load (kgf), e is overall increase in depth of indentation due to major load F_1, measured in units of 0.001 mm, E is a constant of 100 units for diamond and ball indenters, HR is the Rockwell hardness number D is the diameter of steel ball.

Since air plasma spray uses ionized gas plasma to melt and propel the powder, the powders coated on the surface are in the form of small groups, the spaces between powder groups form the pore in the microstructure. Figure 3.3 shows the concept of the formation of pores inside the coatings. Due to the high temperature, oxides can be formed as illustrated in the figure as well. The porosity is in the range of 5-10%, and the oxides contents is about 1-3% of the whole volume.

One of the challenges in finite element modeling thermal barrier coating is the definition of the complex microstructure as mentioned above. Basically, there are two methods to define the structure in finite element simulation. First, make the assumption that the material is homogenous, and assign the material properties correspond-

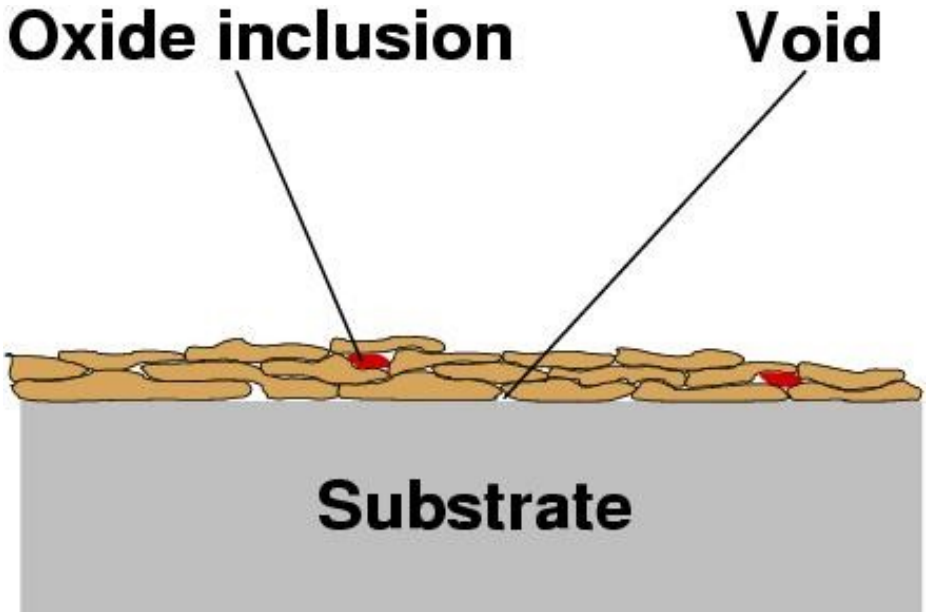

Figure 3.3. Schematic microstructure of thermal spray coating, showing only a few layers of particles [42]

ing to a porous media. Second, maintain the material properties as fully dense, and make the geometry similar to the real structure [43]. Yan et al [43] established both of these two classes of finite element model for columnar structured EBPVD thermal barrier coatings, and compared with experimental results of Rockwell indentation. Fuller et al [44] investigated the thermal properties of thermal barrier coatings using the object oriented finite element method, and then compared the calculated thermal conductivity to experimental data.

The structure of this chapter falls into three parts, section 3.1 shows experimental Rockwell indentation and some of the results. Section 3.2 shows the model validation of microstructure based FEM using Tungsten carbide/Cobalt (WC/Co) matrix structure, starting from microscopic image, to build a finite element model for mechanical property analysis. Section 3.3 performs the Rockwell indentation modeling for YSZ thermal barrier coating using the validated method.

3.2 Experimental Tests and Results

3.2.1 Test Procedure

The HR-15N Rockwell Hardness text was conducted using a Wilson Rockwell hardness testing machine with a standard dimension Brale diamond indenter, displayed in figure 3.4. YSZ coated specimens in addition to NiCoCrY bond coat material were used to investigate the hardness. The specimens were cleaned by using acetone before testing and were dried using a hot air blower. A diamond indenter with load of 15kg was used to indent the specimens. The Rockwell hardness number was recorded and was noted as hardness value for the corresponding specimen.

3.2.2 Results and Discussion

From the indentation test, the hardness of these samples were measured directly by the testing equipment, the mean hardness is 78.06 HRN.

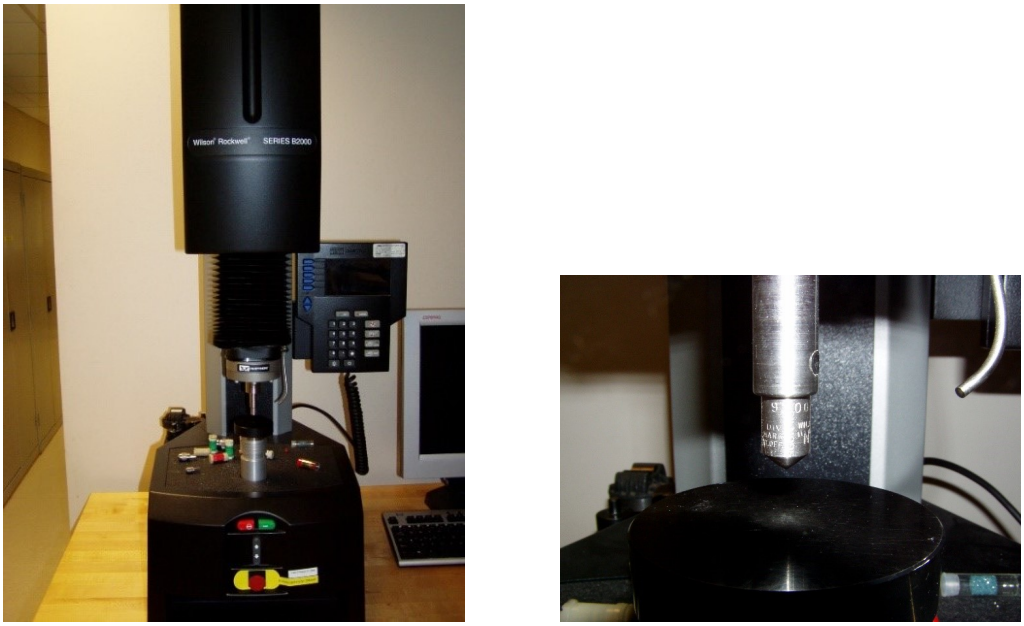

Figure 3.4. Indentation test machine (left) and the Rockwell indenter (right)

Cross section image of APS sprayed thermal barrier coating were also taken by using the microscopic machine; Figure 3.5 shows the layered microscopic structure of the YSZ thermal barrier coating. The gray layer in the middle shows the yttria-stabilized zirconia coating, and the white layer at the bottom shows the alumina bond coat.

Figure 3.5 illustrates the cross sectional structure of YSZ thermal barrier coating. The thickness of YSZ coating is about 500 μm, and the NiCoCrY bond coat is about 200 μm. From this image, the porous structure of coated powders are clearly shown. The small dark regions in both layers show pores inside the sprayed powders. This is due to the process of air plasma spray.

3.3 Validation of Microstructure Based Finite Element Simulation

Tungsten carbide/Cobalt (WC/Co), also named as cemented carbide, is a preferable metal matrix composite (MMC) due to its lightweight and favorable mechanical and thermal behaviors. WC/Co MMC was first produced in the 1920s [45], and it has

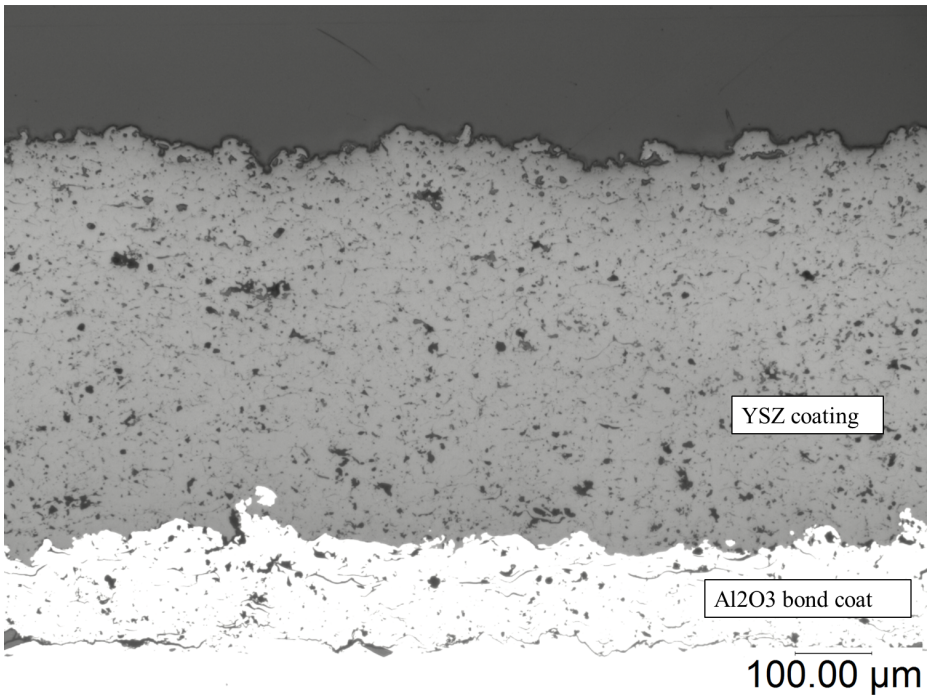

Figure 3.5. Microscopic image of the APS YSZ coating

been the advanced material for rock drilling insert. With the development of technology, based on the conventional cemented carbide, a new microstructure material named DC-carbide it has been applied [46]. WC/Co DC-carbide is a hybrid highly dense particulate metal matrix structure, filled in to a Co metal matrix. The WC/Co particle consolidation component can resist wear in the operation of the material. On the other hand, the ductile cobalt metal matrix leads to a preferable fracture toughness [47, 48].

DC carbides have various specific applications due to their difference in microstructure. That is because material properties may be affected by the microstructure of DC carbides, including particle size, volume percentage of cobalt metal matrix, distribution of particle size, WC particle size and volume percentage of cobalt in the particle. Thus, determining behavior of those materials is important.

Recently, both analytical and numerical models have been developed broadly to investigate and study the properties of multiphase materials [49–57]. For some simple structured material, analytical models can obtain rational predictions. Extending the domain of study, numerical analysis may provide reasonable results for relatively complex model, however, there are also some assumptions that simplified the structure of the MMC: it does not apply for heterogeneous structured materials. The object-oriented finite element technique (OOF) is an advanced finite element analysis approach which conducts microstructure in finite element modeling (FEM) [58, 59]. OOF starts with the 2 dimensional microstructure of the multiphase material, incorporates with basic material properties, and determines mechanical or thermal behaviors of the composite materials. It is well known that conventional FEM builds a unit-cell model, followed with analysis to predict the behavior of material. OOF, however, applies real microstructure of the desired material to proceed finite element analysis.

In this chapter, according to a photo of WC/Co microstructure, a 2D drawing of double-cemented WC particle-reinforced Co matrix composite microstructure was made in Pro/Engineering software, and then this drawing was used to make a finite

element model in ANSYS. Finally, results including coefficient of thermal expansion (CTE) and elastic modulus of this composite material were obtained from the FEM.

3.3.1 Analytical Modeling

Before building OOF models, a theoretical analysis was conducted. This analysis can be divided into two parts: thermal expansion analysis and Young's modulus analysis.

Analytical Modeling of Coefficient of Thermal Expansion

Figure 3.6.shows a photo of the WC particle-reinforced Co matrix composite microstructure; the dark circles represent W/C particle and the light gray shapes are Co matrix. As we can see in Table 3.2, because of the CTE difference between two materials (14.2 for Co and 5.5 for WC), under temperature change, thermal residual stress will occur on the interface.

Table 3.2. Material property of WC/Co composites

Constituent	**Young's Modulus (GPa)**	**Coefficient of Thermal Expansion** ($10^6\ K^{-1}$)	**Poissons Ratio**
Co	209	14.2	0.31
WC	620	5.5	0.22

A comparison between experimental and simulated coefficients of thermal expansion was also conducted. Analytical bounds developed by Turner [51], Kerner [52], and Rosen and Hashin [49] were used as comparison to the experimental data. Rosen and Hashin [49] developed a model to determine the CTE of an isotropic two-phase composite reinforced with spherical particles, in which the spherical reinforcement

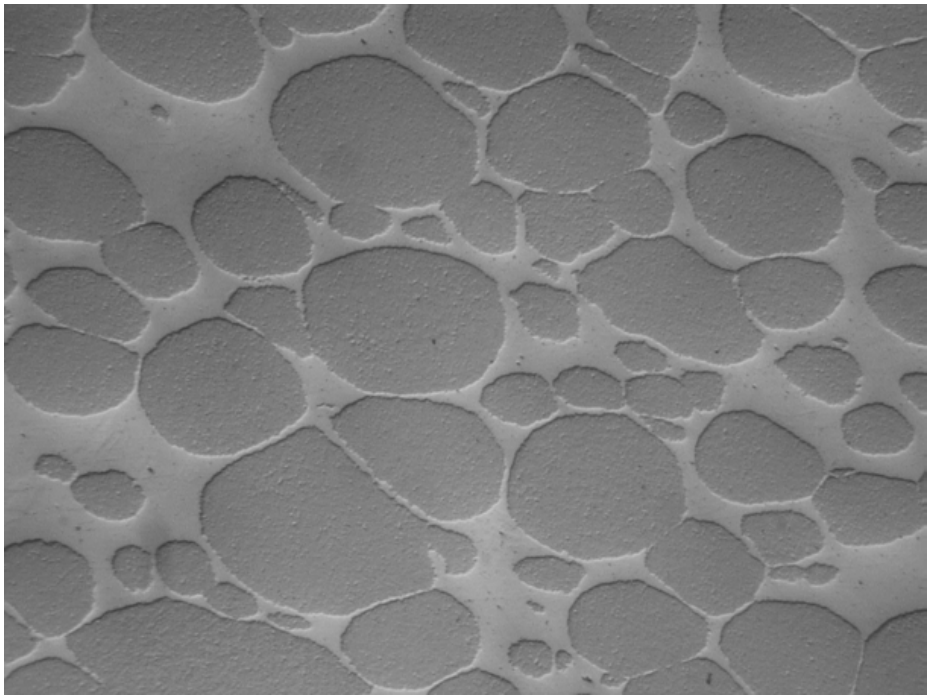

Figure 3.6. Microstructure of Co-WC composite material

was wetted by a uniform layer of matrix. This model (Eq. 3.2) is based on the energy principles of thermo elasticity and on Hashins bounds for bulk modulus of the composite:

$$\frac{4V_mV_pG_p(K_m-K_p)(\alpha_m-\alpha_p)}{3K_mK_p+4G_p\overline{K}} \geq \alpha^* - \overline{\alpha} \geq \frac{4V_mV_pG_m(K_m-K_p)(\alpha_m-\alpha_p)}{3K_mK_p+4G_p\overline{K}} \tag{3.2}$$

$$\overline{K} = \frac{K_pK_m + (4/3)G_m(V_pK_p+V_mK_m)}{V_pK_m+V_mK_p+(4/3)G_m} \tag{3.3}$$

$$\overline{\alpha} = \alpha_mV_m + \alpha_pV_p \tag{3.4}$$

Where V is the volume fraction, G is the shear modulus, K is the bulk modulus, α is the CTE, $\overline{K}$is the bulk modulus of the composite (Eq. 3.3), and $\overline{\alpha}$ is the rule of mixtures CTE (Eq. 3.4). The subscripts m and p denote the matrix and reinforcing constituent. As the case of 2D, V_m and V_p can be substituted as A_m and A_p, which means the area of matrix material (Co) and constituent (WC):

$$\bar{\alpha} = \alpha_mA_m + \alpha_pA_p \tag{3.5}$$

Thus, we can determine the CTE of a composite material only if we know the area ratio of both materials and their CTE in pure state.

3.3.2 Analytical Modeling of Young's Modulus

In this section, we attempt to predict the anisotropy in Young's modulus using two well-known analytical models for predicting modulus of particle reinforced composites: (a) The HashinShtrikman (HS) model [49] and (b) The HalpinTsai (HT) model [60] . The HS model estimates upper and lower bounds for modulus of an isotropic spherical aggregate based on variational principles of elasticity. In the HS model, the Young's modulus was calculated from the upper and lower bounds of the bulk moduli, K upper and K lower, and shear moduli, G upper and G lower, of the composite:

$$K_{upper} = K_R + (1-V_p)\left[\frac{1}{K_M-K_R} + \frac{3V_p}{3K_R+4G_R}\right]^{-1} \tag{3.6}$$

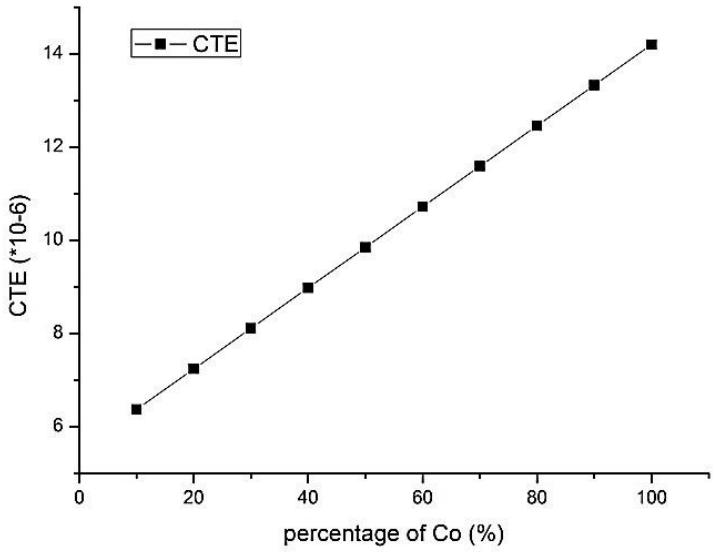

Figure 3.7. CTE and percentage relation of Co in composite

$$K_{lower} = K_M + V_p\left[\frac{1}{K_R - K_M} + \frac{3(1-V_p)}{3K_M + 4G_M}\right]^{-1} \tag{3.7}$$

$$G_{upper} = G_R + (1-V_p)\left[\frac{1}{G_M - G_R} + \frac{6V_p(K_R + 2G_R)}{5G_R(3K_R + 4G_R)}\right]^{-1} \tag{3.8}$$

$$G_{lower} = G_M + V_p\left[\frac{1}{G_R - G_M} + \frac{6(1-V_p)(K_M + 2G_M)}{5G_M(3K_M + 4G_M)}\right]^{-1} \tag{3.9}$$

where V_p is the volume fraction of the reinforcement, and M and R represent the matrix and reinforcement, respectively. The upper and lower bounds of the Young's modulus for each component can then be calculated using the following relation:

$$E = \frac{9K}{1 + (3K/G)} \tag{3.10}$$

The HT model, on the other hand, is a semi-empirical model that assumes a perfectly oriented discontinuous reinforcement in the composite, parallel to the applied load. The Young's modulus of the composite per the HalpinTsai model is given by:

$$E_c = \frac{E_m(1 + 2sqV_p)}{1 - qV_p} \tag{3.11}$$

where E_c is the Young's modulus of the composite, E_p the elastic modulus of the particle, Em the modulus of the matrix, and q can be written as:

$$q = \frac{(E_p/E_m) - 1}{(E_p/E_m) + 2s} \tag{3.12}$$

where s is the aspect ratio of the particle. This model assumes that all particles are perfectly aligned with respect to the loading axis.

A comparison of the experimental data with the analytical predictions is shown in Figure 3.8. As expected, the experimental data fall between the HS upper and lower bounds. There is a fairly wide range between the bounds, due to the large difference in Young's moduli of the components of the composite.

3.3.3 Microstructure Based Modeling

The analysis above shows that in order to quantify the anisotropy in modulus, as well as an understanding of the local stress and strain states, the microstructure

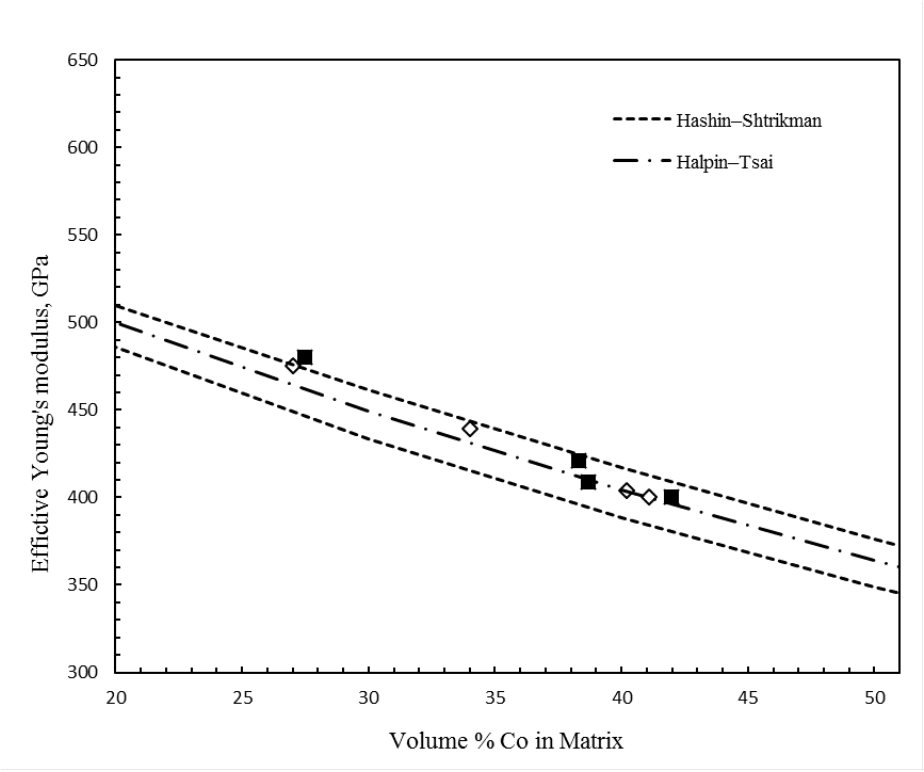

Figure 3.8. Experimental and computational results follow a similar decreasing trend in Young's modulus with increasing matrix Co content

of the composite needs to be incorporated into the model. Relatively few studies have used multiparticle models using an FEM approach [61,62]. In these studies, the particle shape was simplified and the aspect ratio and orientation approximated from the microstructure. Although these models were able to qualitatively account for the orientation and distribution of the particles, a true representation of the microstructure must capture the inherent heterogeneity and complexity of the microstructure, particularly since the WC particles are highly angular and often distributed inhomogeneously. In this regard, we have incorporated the actual microstructure of the composite, using a two-dimensional analysis, to obtain an understanding of composite behavior and to predict the experimentally observed anisotropy in Young's modulus. Modeling of the deformation behavior of the composites materials was carried out using a microstructure-based finite element modeling technique. Digital micrographs obtained from SEM were used as input for elastic analysis using a commercial finite element software, ANSYS. A representative area of the microstructure was sketched manually using computer aided design software Pro/Engineer (Fig. 3.9). The segmented microstructure was converted to an exchangeable drawing file, and imported to the FEM software for analysis.

Microstructure Geometry Modeling

In order to achieve the geometry for finite element analysis, a sketch was drawn in Pro/Engineer CAD software manually. The completed sketch can be seen in fig. 3.9.

Microstructure Geometry Validation

As mentioned above, this study analyzed both thermal expansion and elastic modulus. The parameter that determines the result of CTE and E is the area ratio of each material. It is important to validate the area ratio of both materials in the microstructure CAD drawing. In this paper, the area ratio of different materials was

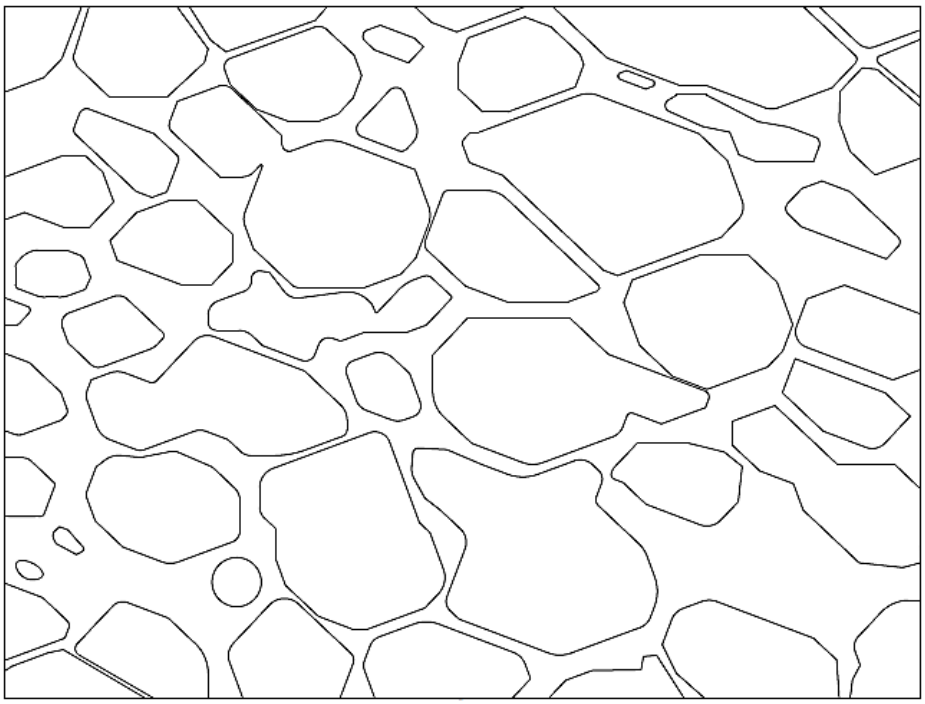

Figure 3.9. Sketch created in Pro/E

calculated as soon as it was imported into ANSYS; for the structure in Fig. 3.9 , the area ratio of Co is 32.4% of the whole structure by the calculation of ANSYS.

On the other hand, in order to validate the CAD drawing, a paper weighting process was conducted as well. The steps of this process included: print the microstructure photo on a paper followed by weighting the paper, and then cut off the Co particle pieces on the paper and then weigh the particle paper pieces. By doing the above steps, the weight of the whole structure and the weight of the Co particle were achieved. Thus, the percentage of Co matrix in the composite material can be calculated as below:

$$Co_{percentage} = \frac{weight_{matrix}}{weight_{whole}}\% = \frac{0.90g}{2.97g}\% = 30.3\% \tag{3.13}$$

As the Co percentage results from the above two ways, the error of the microstructure geometry modeling is about 7%, which means the geometry was properly modeled.

Microstructure Based Finite Element Modeling

Firstly, import the drawing from Pro/E into ANSYS as mentioned in the above section, and modify the lines in order to complete individual areas shown in Fig. 3.10 The circular areas represent WC particles whereas the matrix area represents the Co matrix.

Material properties used in the model are shown in Table 3.3. Both cobalt matrix and tungsten carbide were modeled as linear elastic materials with Young's modulus and Poissons ratio. PLANE183 element type was applied to this model. Fig. 3.11 shows a magnified view of the highly dense mesh of the microstructure of a WC/Co structure. The light blue area is meshed by Co material and the dark ones are meshed by WC. One of the analyses was carried out in plane stress state and a 700K temperature elevation from 0^oC was applied to all models (Fig. 3.12). And the other analysis was a 1.0% uniaxial tensile strain applied along the horizontal direction on the plane (Fig. 3.13).

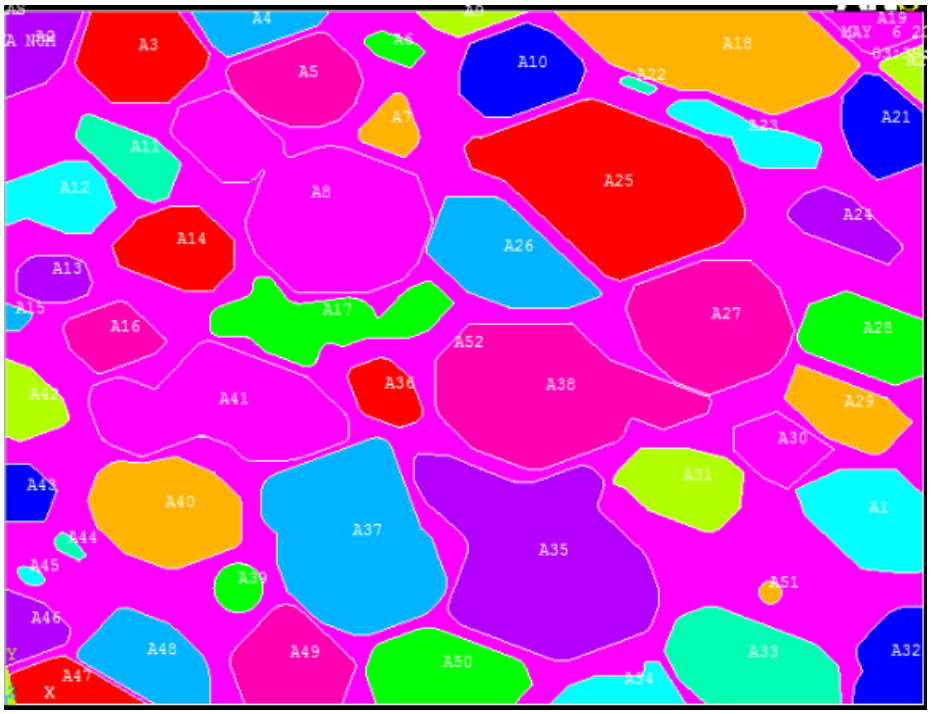

Figure 3.10. Area created in ANSYS according to the microstructure

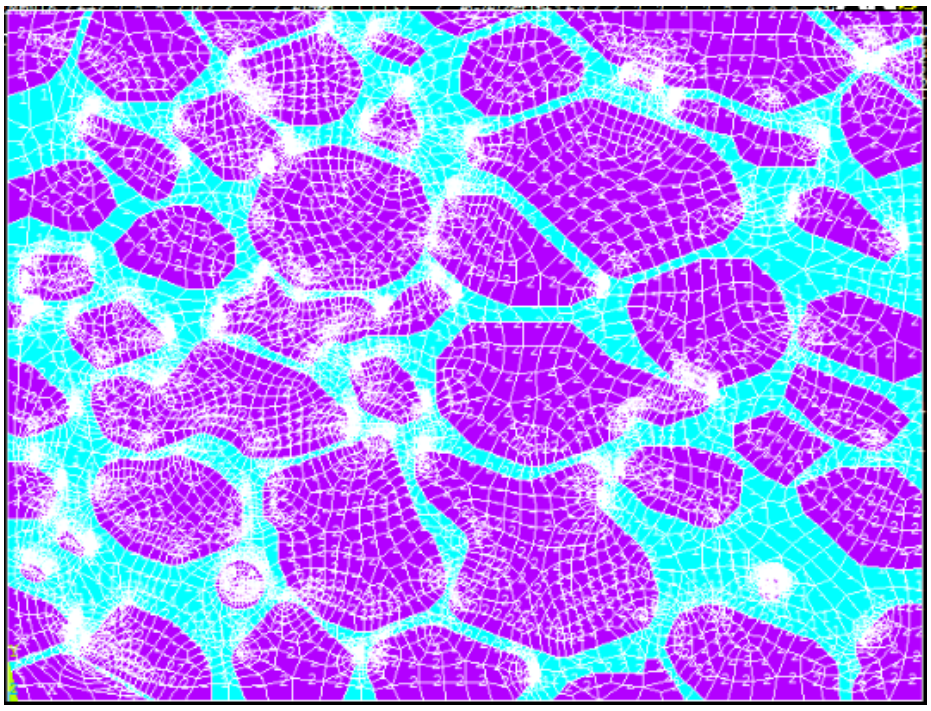

Figure 3.11. Mesh used in the model

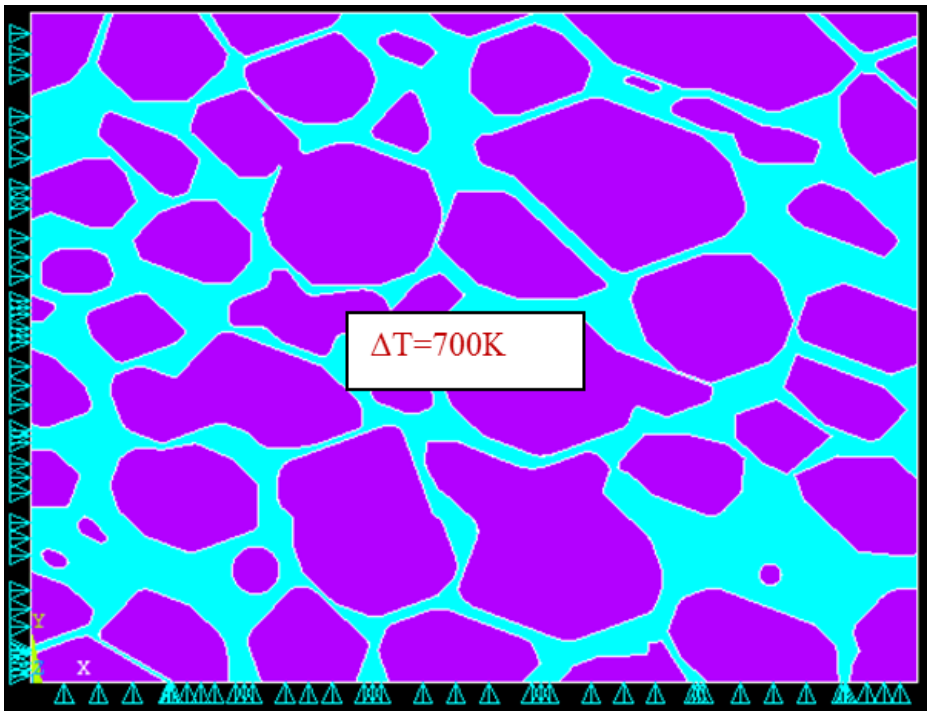

Figure 3.12. Boundary conditions for temperature elevation test

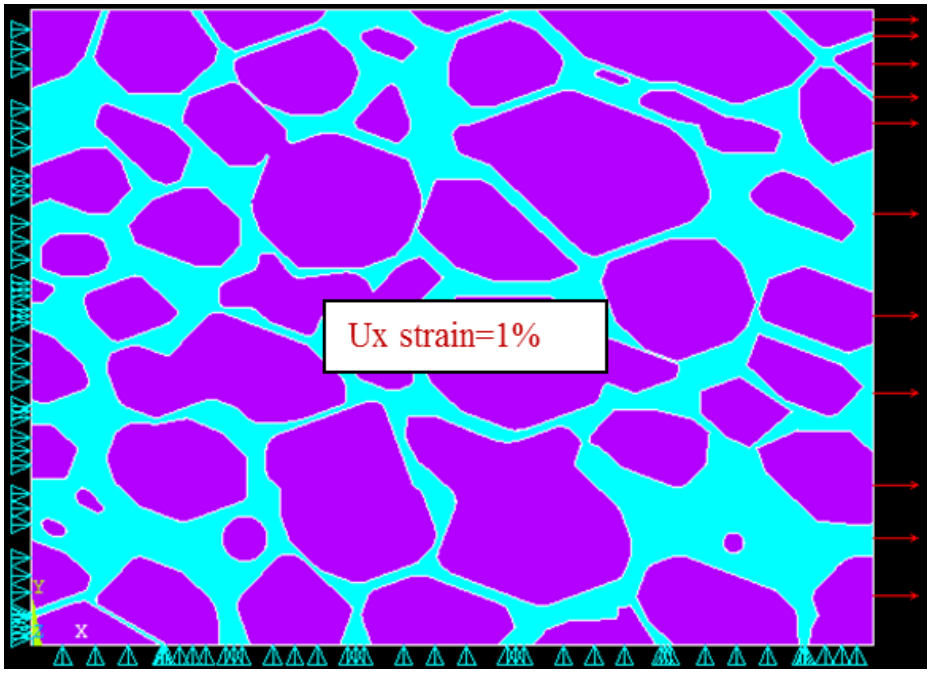

Figure 3.13. Boundary conditions for uniaxial tensile test

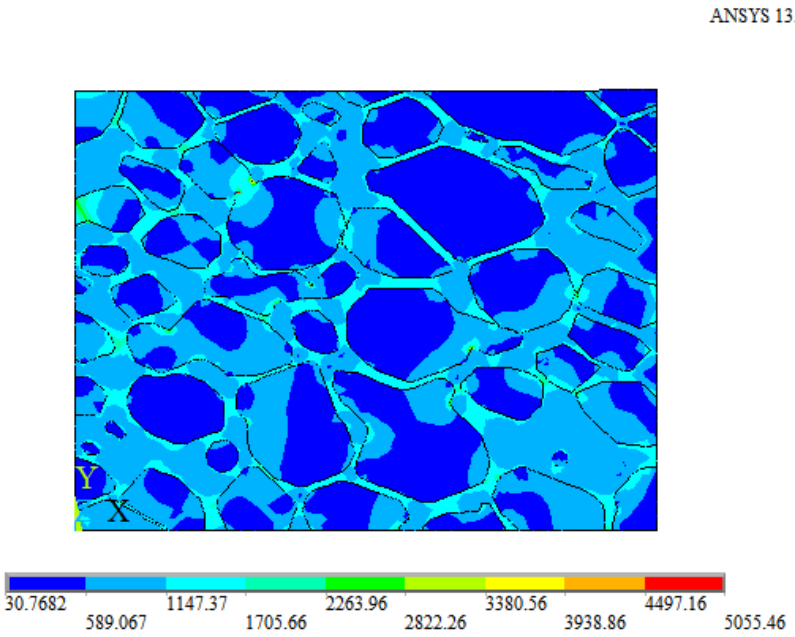

Figure 3.14. von-Mises stress under 700K temperature increasing

3.3.4 Results and Discussion

Temperature Elevation Test

After appling 700 K increment of temperature, the thermal stress can be shown in fig. 3.14. From this figure we can see: because of the higher elastic modulus, WC components had lower stress than that of Co; the stress changed gradually along the interface between the two materials; there were no sharp edges on the geometries, so that there was not any stress concentration.

The objective of thermal expansion test is to determine the CTE by getting the elongation of the model. The elongations along both x and y directions are shown below: (fig.3.15)

By the definatin of CTE, one can use the elongation data and equation (3.14) to calculate the CTE of this composite material.

$$\alpha = \frac{1}{L}\frac{\Delta L}{\Delta T} \tag{3.14}$$

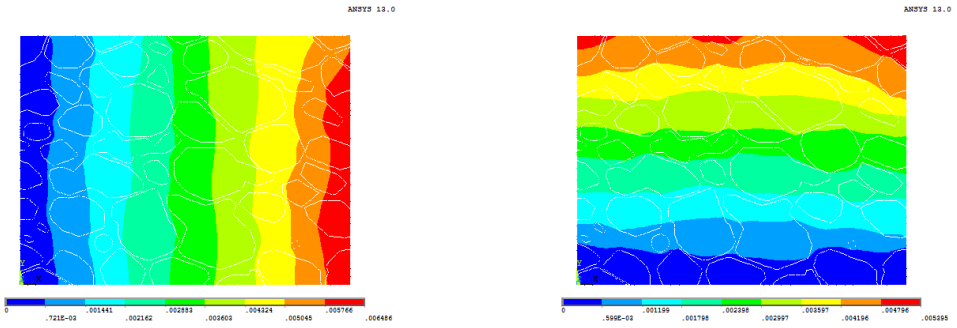

(a) (b)

Figure 3.15. Elongation along x (a) and y (b) directions

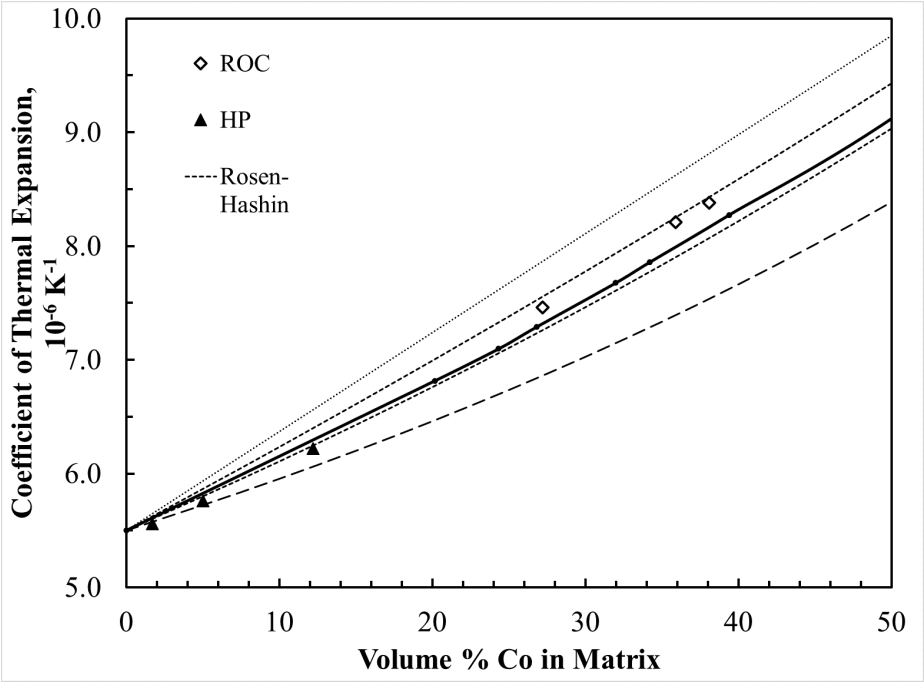

Figure 3.16. Simulated and calculated coefficient thermal expansion

Further, by modeling photos with different percentage of Co, the result of Co percentage versus CTE on each direction were obtained, then compared with the result in theoretical analysis (fig. 3.16):

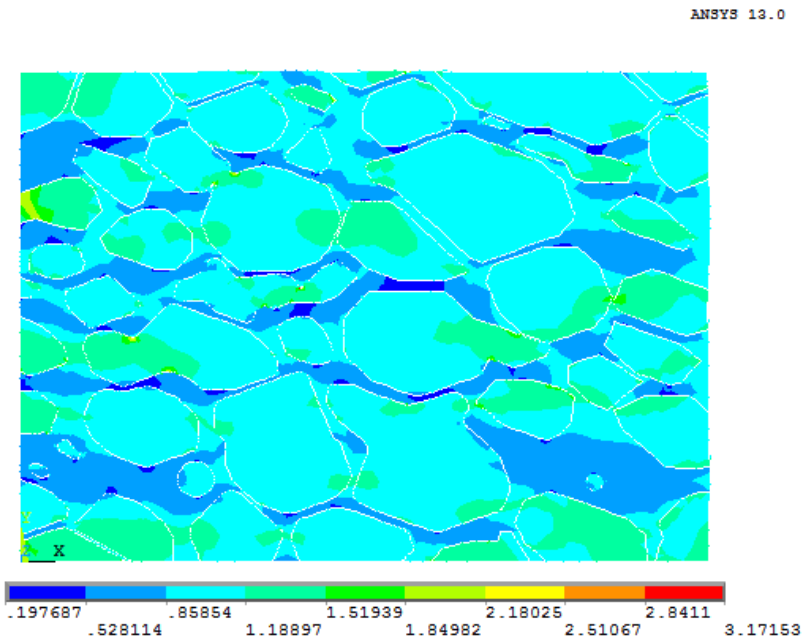

Figure 3.17. von-Mises stress of the tensile result

At 0% Co, the CTE is 5.5×10^{-6} for both simulated and calculated results, respectively; this means that the tested model is a pure WC material model. In the 100% case, it is pure Co material and CTE is 14.2×10^{-6}. The model results are close to the calculated results during the change of the Co matrix ratio in the Co/WC composite material.

Uniaxial Tensile Test Results

In the tensile test, the aim is to measure the elastic modulus (E) and Poissons ratio (v) of the composite material. The method is to get the simulated elongation result in x direction for E, and y for v, then calculate using the equation 3.15. Von-Mises stress of tensile test model is shown in Fig. 3.17. Similar to the thermal extrusion simulation, the stress changed gradually along the interface between the two materials; there were no sharp edges on the geometries.

$$E = \frac{stress}{strain} = \frac{PL}{\Delta L} \tag{3.15}$$

Elongations on the x direction is a positive value because the tensile is along x direction, whereas the y axis elongation is a negative value. They are shown in fig.3.18:

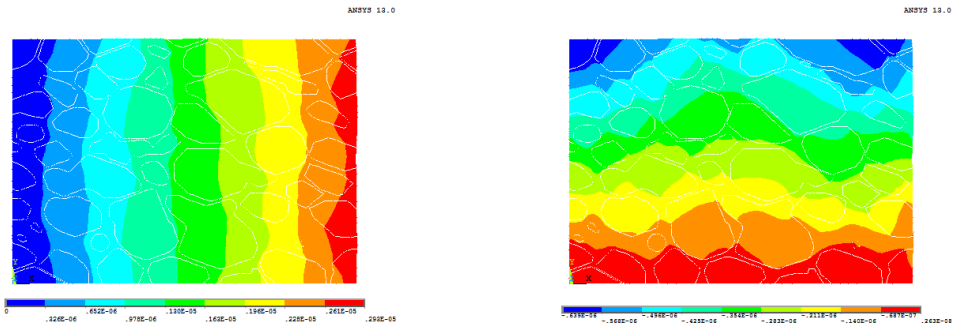

(a) (b)

Figure 3.18. Elongation along x (a) and y (b) directions

Fig. 3.19 shows simulated E on x and y direction based on different percentages of Co are processed then compared with analytical result calculated from equation 3.14.

From Fig. 3.8, At 0% Co, the elastic modulus is 618 GPa and 620 MPa for simulated and calculated results respectively, this means that the tested model is a pure WC material model. In the 100% case, it is pure Co material and elastic moduli are 209GPa. The model results are close to the calculated results during the change of the Co matrix ratio in the Co/WC composite material.

3.3.5 Summary

Object-oriented finite element analysis (OOF) can be used as an effective tool for evaluating material behavior under thermal and/or elastic conditions, because it incorporates the inherent microstructure of the material as an input to the model. OOF was successfully used to predict Young's modulus and CTE in two multiphase

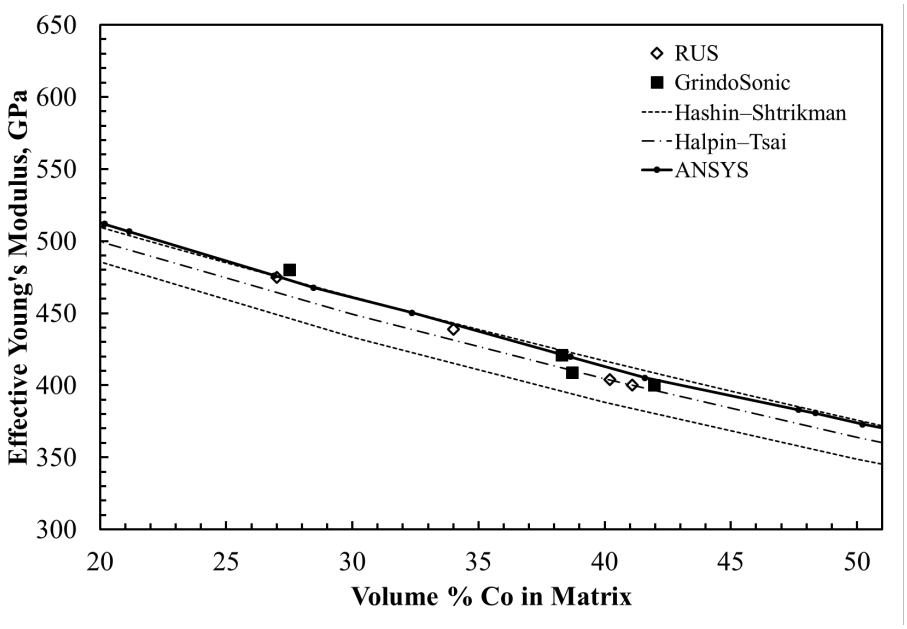

Figure 3.19. Analytical calculated and simulated Young's Modulus

systems. Conclusions obtained from OOF modeling are shown below: 1). In the rise of temperature, increasing volume percentage of the Co matrix leads to a linear growth of CTE of the DC carbide composite material. CTE of the composite material increases from 5.5×10^{-6}, the CTE of pure WC, to 14.2×10^{-6}, the CTE of pure Co, as the volume percentage of Co rises from 0 to 1002). Under tension, increasing volume percentage of Co matrix contributes to a nonlinear rise of Young's modulus of the DC carbide. At 0 and 100 volume percent, E agree with the Young's modulus of pure WC particles and Co matrix, respectively. In the range between 0 and 100%, E fits in the prediction of analytical analysis.

3.4 Finite Element Modeling of Rockwell Indentation

As the method of object oriented finite element analysis was validated, the air plasma sprayed YSZ coating with bond coat as the sample of Rockwell indentation test was simulated using object oriented FEM. Mechanical behaviors of YSZ coating under indentation conditions, pre-loading, after loading, after unloading, were simulated and analyzed. The microscopic image of YSZ coating was processed and imported into Commercial FEM software ANSYS. The Rockwell indenter geometry was created and simulated as a rigid surface in the contact pair. Large deformation were assumed in the computational model. The calculations were based on static structural non-linear analysis.

3.4.1 Image Processing

This simulation is based on the microscopic image in figure 3.20. Figure 3.20 shows the three layers of the YSZ thermal barrier coating structures, including air (on the top, no material properties will be applied in this area), YSZ (in the middle), and the bond coat made by NiCoCrY. Obviously in this figure, there are many small holes in the YSZ layer and the bond coat; the purpose for image processing is to convert this image to a geometry for finite element modeling, and these holes will make the

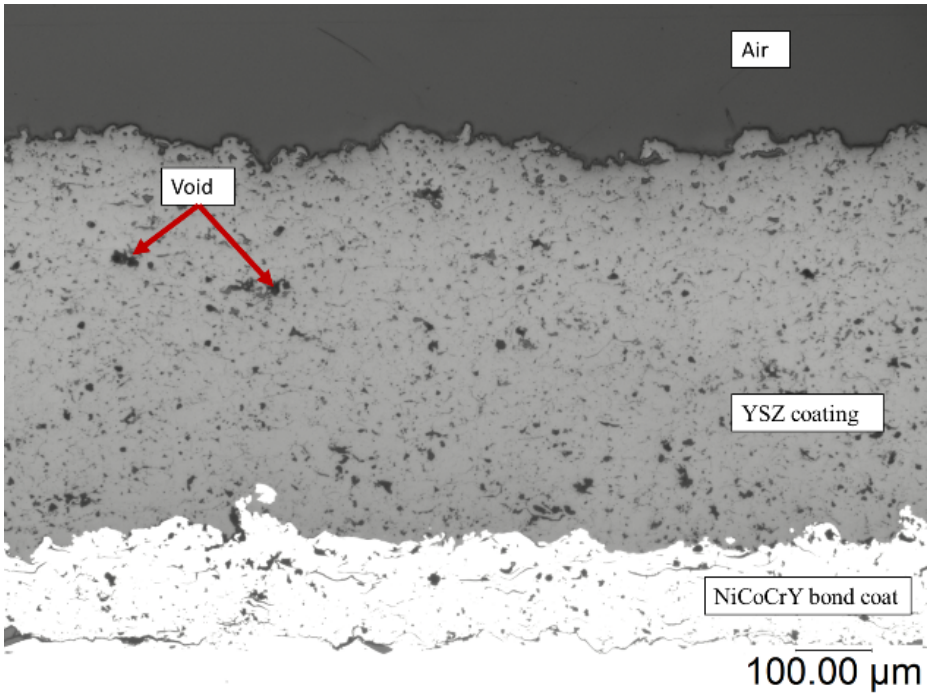

Figure 3.20. Microscopic image of yttria-stabilized zirconia and groups defined for modeling

geometry very complex. Due do the computational time cost, it is impractical to build the exactly same FEM model with the microscopic image, so modifications and simplifications are needed. The basic simplification method can be seen in figure 3.21; there are two types of void: the bigger ones, which are compatible with FEM modeling; and the smaller ones, which may cause problem for meshing. For the bigger type of void, their location and area were kept for sketching, and the effect of the smaller ones are attributed to the material properties (elastic modulus) in the model.

A simplified microscopic image was manually sketched in FEM package ANSYS. By extruding the sketch, a three dimensional TBC coating, with the thicknesses of 0.2 mm bond coat and 0.5 YSZ top coat, was built in the FEM package as shown in figure 3.21, then an indenter according to the tip of Rockwell HR-15N indenter dimension [63] was created on top of the TBC layers, see figure 3.22.

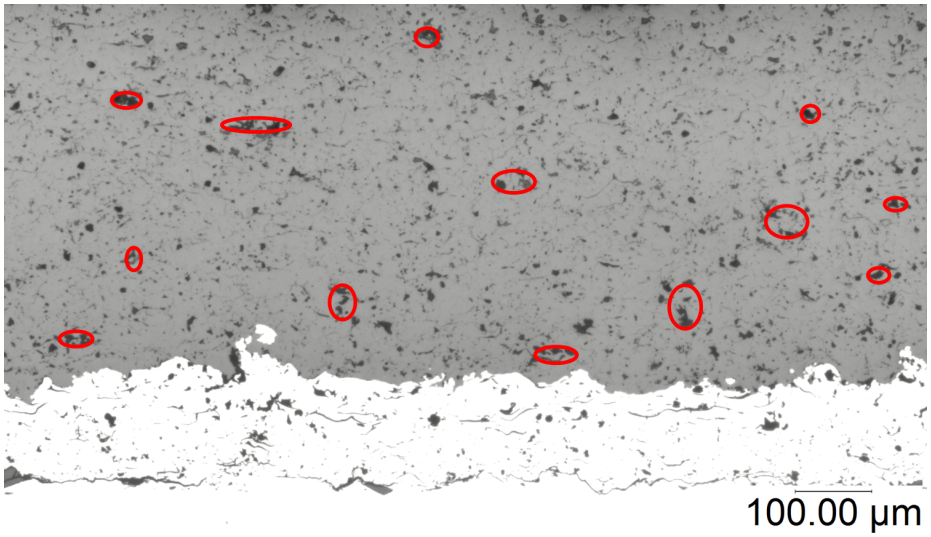

Figure 3.21. Schematic of the methods used in image processing (red holes will be modeled in the FEM geometry, porosity caused by other holes will be complimented by the material properties)

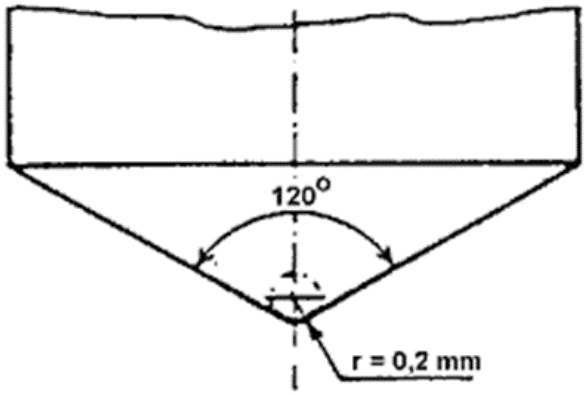

Figure 3.22. Dimensions of a standard Rockwell indenter for HR-15N hardness test.

3.4.2 Material Properties

Two types of materials were simulated in this model, yttria-stabilized zirconia top coat and aluminum oxide bond coat. The material properties used in this model are shown in Table 6. Both homogenous material and image based material were simulated. For the case of the image based model, all the material properties were defined according to the Table 3.3; for the case of the homogenous model, 10% of the Young's modulus was reduced due to the porosity identified in the image.

Table 3.3. Material properties defined in the FE simulation

Material	**Distribution**	**E(GPa)**	ν	σ
YSZ	top coat	250 [64]	0.3	3000
NiCoCrY	bond coat	190 [65]	0.3 [64]	900 [65]
diamond	indenter	1140	0.07	elastic

3.4.3 Model Description

The models in this study are three dimensional solid static analyses. Both the homogenous model and the image based model were simulated in ANSYS workbench. For the sake of computation simplification, one fourth of the entire model was simulated. Figure. 3.23 and 3.24 show the boundary conditions of the models; the bottom faces were fixed at y direction, and the pressure of corresponding to the preloading force of 29.4N was applied to the diamond indenter for one second, then the pressure corresponding to the loading force of 147N was further applied on the indenter for one second. Finally, the loading force was removed, and the indenter was balanced at the unloaded depth. The load steps of this simulation are shown in figure 3.25

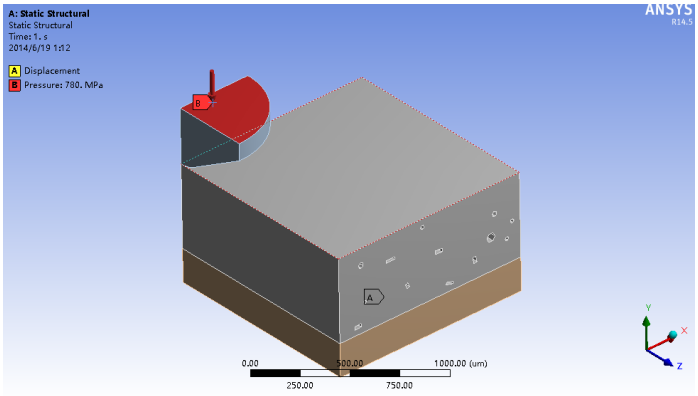

Figure 3.23. Geometry and boundary conditions of the image based model

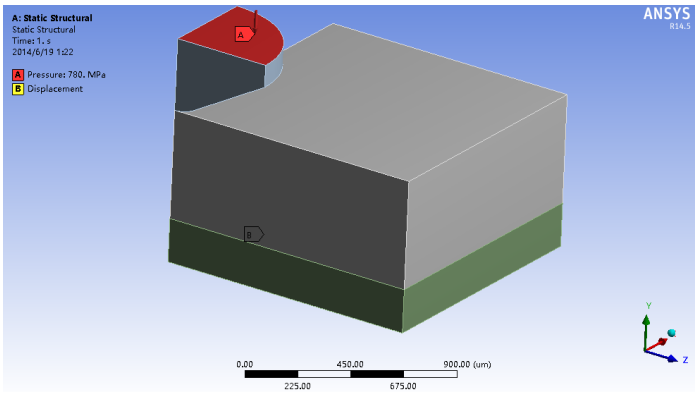

Figure 3.24. Geometry and boundary conditions of the homogenous model

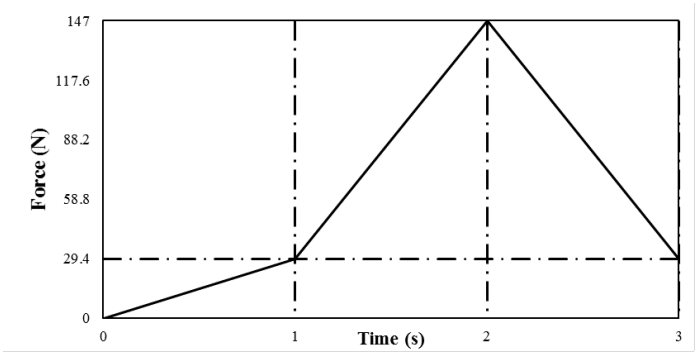

Figure 3.25. Loadsteps of Rockwell indentation according real test

3.4.4 Results and Discussion

von-Mises stress distribution of both simulations are shown in figures below. Figures 3.26 (a) and (b) show the homogeneous model under loading and after unloading. Under loading, the stress was concentrated at the bottom of the indenter tip, due to the compressive pressure provided by the indentation force; after unloading, the highest stress region was located at the edges of the indentation mark, since the edge materials were compressed during unloading. In figure 3.27(a) and (b), the stress distribution followed the same trend of the homogeneous ones. However, the maximum stress was higher than the former, since the irregular shaped voids attributed to the local stress concentration.

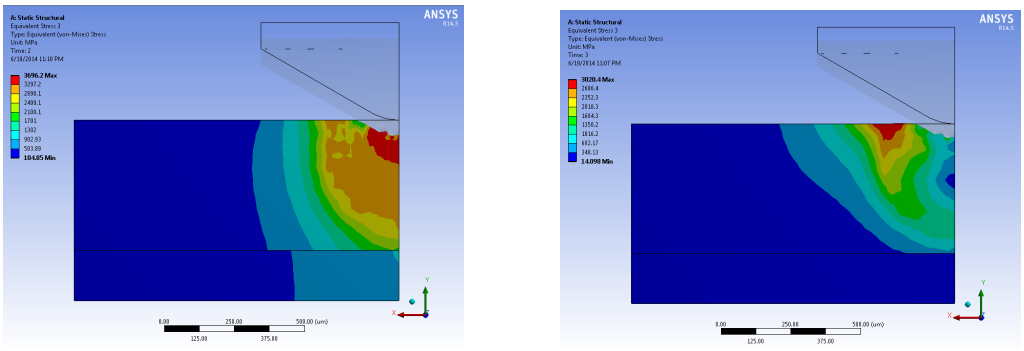

(a) von-Mises stress at the end of 147N loading

(b) von-Mises stress at the end of unloading

Figure 3.26. von-Mises stress distribution (homogeneous material)

Figure 3.28 show more details of stress concentration in the image based model. In figure 3.28 (a), the highest stress is located around the edge of the indentation mark. However, in figure 3.28 (b), the highest stress is located at the top right void which is highly deformed.

Figure 3.29 shows the indentation depth versus the load applied. Since both of the two models are aimed to simulate the 10% porosity YSZ sample, there was not any big difference between the two load-depth curves.

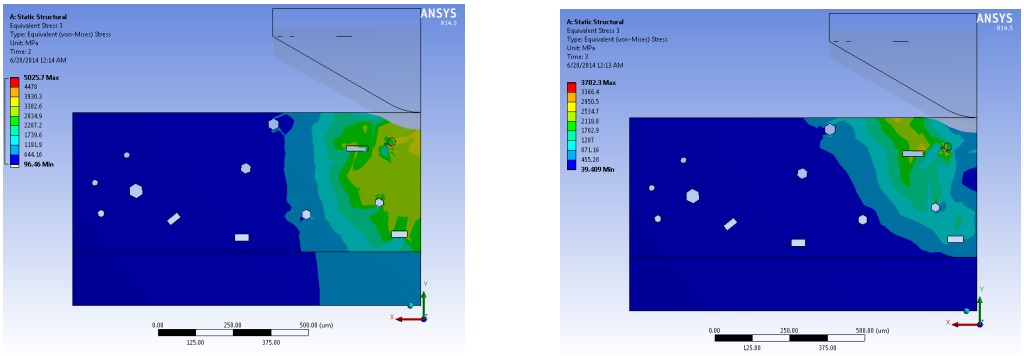

(a) von-Mises stress at the end of 147N loading

(b) von-Mises stress at the end of unloading

Figure 3.27. von-Mises stress distribution (image based)

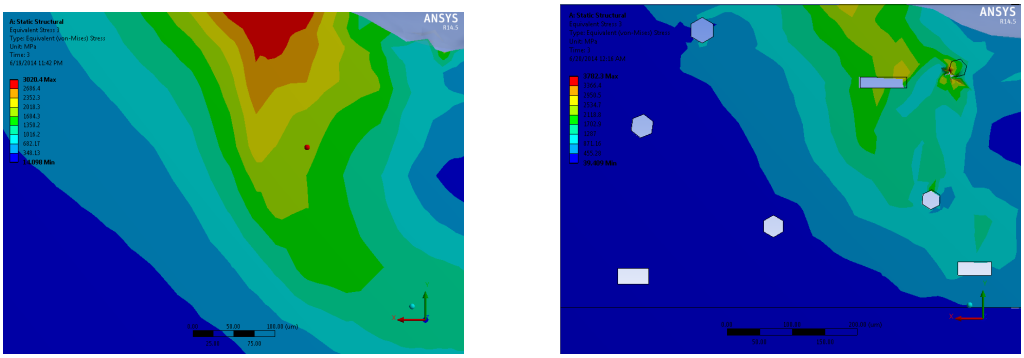

(a) homogenous

(b) image based

Figure 3.28. Localized von-mises stress distribution after unloading

The size of indentation mark visually determines the impact of the indenter on the sample. It can briefly reveal the hardness of the sample; simulated indentation marks and the experimental indentation mark are compared in the following figures. From the figures below, the simulated marks are a little bigger than the experimental mark, this means the simulated hardness may be smaller than the experimental. The comparison of hardness will be discussed later.

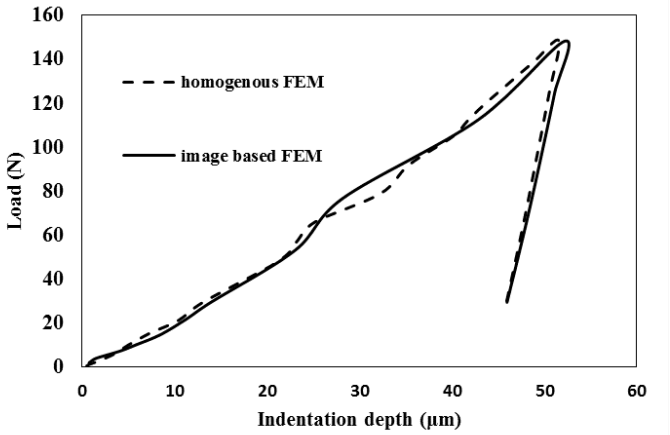

Figure 3.29. Indentation depth versus load

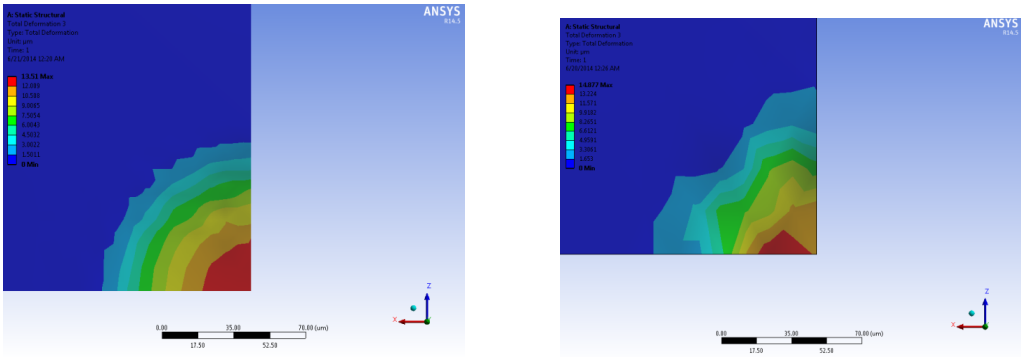

(a) homogenous (b) image based

Figure 3.30. Simulated indentation mark

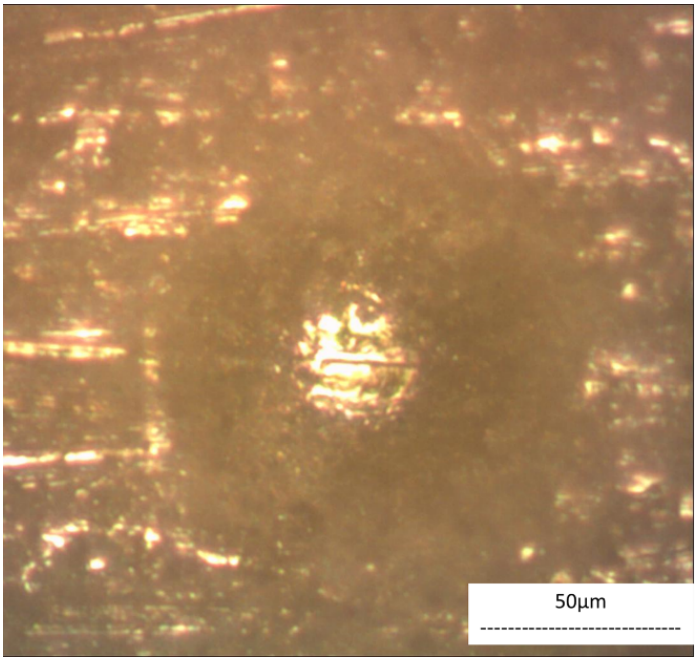

Figure 3.31. Experimental indentation mark image

As mentioned in the beginning of this chapter, the hardness can be calculated by the indentation depth before loading and after unloading. The simulated Rockwell hardness is listed in Table 3.4 and compared with the experimental result.

Based on the comparison, the model for hardness under predicted the result. One of the possible reasons is that the material properties defined in the numerical

Table 3.4. Comparison of the indentation results

	Experimental	**homogeneous**	**image based**
Hardness	78.06	67.204	67.975
Deviation		0.139073	0.129195

model were not accurate enough. For ceramic materials, any microstructure difference might cause the properties in the large scale. Another potential reason is that the indenter used for this indentation test might have wear effect during operation, thus the indentation depth would be under measured, as shown in Eq (3.1), and the real hardness will be smaller than the measured value.

3.5 Summary

In this chapter, a study on Rockwell indentation of yttria-stabilized zirconia was conducted on both experimental and computational aspects. The experimental Rockwell superficial indentation test showed the hardness of YSZ coating was 78HRN and the microscope image was taken for further simulation modeling. The principle of object oriented finite element modeling was proposed and validated using tungsten carbide composite material. Finally, using the microstructure image from the experiment and the validated method, the Rockwell indentation was simulated using finite element analysis, the simulated hardness was close to the experimental data, and analysis was conducted on the aspects of stress distribution and load depth curve.

4. CONCLUSION AND FUTURE WORK

Atomistic scale simulations for both tetragonal and monoclinic phase zirconia were developed. These simulations were based on the first principles method density functional theory. Using this model, thermodynamic properties of monoclinic zirconia crystal structure were first calculated. The specific heat capacity at constant volume kept increasing from 0 to 350 K, from 0 to about 60 J/mol-K, respectively. Comparison of this result with experimental data and simulated results show high agreement. Also by using this model, the temperature dependent phase transition was studied. A monoclinic zirconia unit cell was subjected to compressive hydrostatic pressure up to 50 GPa. Bond gaps were calculated and analyzed. The initial bond gap kept decreasing until the phase transition pressure of 37 GPa; at higher pressures, the bond gap started to increase corresponding to pressure. Lattice geometry was also studied in this model; the tetragonal distortion factor kept decreasing, until it reached a constant value which is not affected by the increasing of pressure. Both the bond gap values and tetragonal distortion factor results indicated the pressure point for phase transition.

Finite element simulation for yttria-stabilized zirconia mechanical properties was conducted. The numerical model of Rockwell indentation was developed using the image-based finite element method. Unlike the conventional finite element modeling, where a homogenous material is defined in the simulation, the image-based FEM started with the microscopic morphology of the TBC material. Because this study took the microstructure of the material into consideration, more accurate results were achieved. The experimental indentation test was performed using Rockwell HR15N superficial indentation, and hardness of YSZ samples were measured. The concept of image based (object oriented) finite element analysis was proposed and the method was well validated by the study of Co/WC matrix structure. The process of validation

included temperature elevation simulation for thermal properties validation, and the tensile stress simulation for mechanical validation. Results show that the image based FEM is good for both thermal and mechanical properties simulations. Finally, this work used the validated image based FEM to simulate the mechanical behavior of YSZ under Rockwell hardness test. The load steps according to the experimental test was simulated and the hardness of YSZ was calculated.

In summary, the new contributions of this thesis work include:

(1) The atomistic simulations correctly predicted the phase transitions of m-ZrO_2 under compressive pressures ranging from 0 to 70 GPa. The phase transition pressures of monoclinic to orthorhombic I (3 GPa), orthorhombic I to orthorhombic II (8 GPa), orthorhombic II to tetragonal (37 GPa), and stable tetragonal phases (37-60 GPa) are in excellent agreement with experimental data.

(2) This work developedan image-based finite element model to simulate Rockwell indentation of air plasma sprayed YSZ thermal barrier coating. The predicted hardness agrees fairly well with the experimentally measured value.

Though significant results have been achieved in this work, there are still many questions that need to be addressed. A few suggested future research directions may include:

(1) Atomistic model of phase transformation of yittria-stabilized zirconia;

(2) Atomistic model of vacancy and defects in zirconia, and their role in affecting material properties;

(3) Three-dimensional finite element model with realistic microstructures.

LIST OF REFERENCES

LIST OF REFERENCES

[1] D.R. Clarke, M. Oechsner, and N.P. Padture. Thermal-barrier coatings for more efficient gas-turbine engines. *MRS Bulletin*, 37(10):891–898, 2012.

[2] J.H. Perepezko. The hotter the engine, the better. *Science*, 326(5956):1068–1069.

[3] R.A. Miller. Thermal barrier coatings for aircraft engines: History and directions. *Journal of Thermal Spray Technology*, 6(1):35–42, 1997.

[4] R.A. Miller. History of thermal barrier coatings for gas turbine engines, 2007.

[5] S Stecura. Experiences in seeking stabilizers for zirconia having hot corrosion-resistance and high temperature tetragonal (t') stability. In *NASA TM-78976, National Aeronautics and Space Administration.*

[6] N.P. Padture, M. Gell, and E.H. Jordan. Thermal barrier coatings for gas-turbine engine applications. *Science*, 296(5566):280–284, 2002.

[7] D.R. Clarke and S.R. Phillpot. Thermal barrier coating materials. *Materials Today*, 8(6):22–29, 2005.

[8] R.L. Jones. Experiences in seeking stabilizers for zirconia having hot corrosion-resistance and high temperature tetragonal (t') stability. Report, Naval Research Laboratory, 1996.

[9] K. Vaidyanathan. *Failure mechanisms of platinum aluminide bond coat/electron beam-physical vapor deposited thermal barrier coatings.* Thesis, 2001.

[10] R. Vassen, X. Cao, F. Tietz, D. Basu, and D. Stver. Zirconates as new materials for thermal barrier coatings. *Journal of the American Ceramic Society*, 83(8):2023–2028, 2000.

[11] J. E. Burke. Ceramics today. *Science*, 161(3847):1205–12, 1968.

[12] M. H. Bocanegra-Bernal and S. D. De la Torre. Phase transitions in zirconium dioxide and related materials for high performance engineering ceramics. *Journal of Materials Science*, 37(23):4947–4971.

[13] S. Block, J. A. H. Da Jornada, and G. J. Piermarini. Pressure-temperature phase diagram of zirconia. *Journal of the American Ceramic Society*, 68(9):497–499, 1985.

[14] H. Yanagida, K. Kmoto, and M. Miyayama. *The chemistry of ceramics.* Wiley, 1996.

[15] D.R. Clarke. Materials selection guidelines for low thermal conductivity thermal barrier coatings. *Surface and Coatings Technology*, 163164(0):67–74, 2003.

[16] Accelrys Materials Studio 6.1. 2012.

[17] A. Kuwabara, T. Tohei, T. Yamamoto, and I. Tanaka. Ab initio lattice dynamics and phase transformations of zro2. *Physical Review B*, 2005.

[18] X.Y. Zhao and D. Vanderbilt. Phonons and lattice dielectric properties of zirconia. *Physical Review B*, 65(7):075105, 2002.

[19] T. Tojo, T. Atake, T. Mori, and H. Yamamura. Heat capacity and thermodynamic functions of zirconia and yttria-stabilized zirconia. *Journal of Chemical Thermodynamics*, 31(7):831–845, 1999.

[20] X. Luo, W. Zhou, S. Ushakov, A. Navrotsky, and A. Demkov. Monoclinic to tetragonal transformations in hafnia and zirconia: A combined calorimetric and density functional study. *Physical Review B*, 80(13), 2009.

[21] G.M. Rignanese. Dielectric properties of crystalline and amorphous transition metal oxides and silicates as potential high- candidates: the contribution of density-functional theory. *Journal of Physics: Condensed Matter*, 17(7):R357, 2005.

[22] H. ztrk and M. Durandurdu. High-pressure phases of zro2: An ab initio constant-pressure study. *Physical Review B*, 79(13):134111, 2009.

[23] M. Victor, P. Alexander, R. Keith, J.C. Stewart, G. Jacob, and W. Bjoern. Structural, electronic and vibrational properties of tetragonal zirconia under pressure: a density functional theory study. *Journal of Physics: Condensed Matter*, 21(48):485404, 2009.

[24] J.E. Jaffe, R.A. Bachorz, and M. Gutowski. Low-temperature polymorphs of zro2 and hfo2: A density-functional theory study. *Physical Review B*, 72(14):144107, 2005.

[25] O. Ohtaka, T. Yamanaka, and T. Yagi. New high-pressure and temperature phase of zro2 above 1000 c at 20 gpa. *Physical Review B*, 49(14):9295–9298, 1994.

[26] E.Y. Tonkov. *High Pressure Phase Transformations: A Handbook*. Gordon and Breach Science Publishers, 1992.

[27] E.R. Leite and C. Ribeiro. *Crystallization and Growth of Colloidal Nanocrystals*. Springer, 2011.

[28] H. Arashi, T. Yagi, S. Akimoto, and Y. Kudoh. New high-pressure phase of zro2 above 35 gpa. *Physical Review B*, 41(7):4309–4313, 1990.

[29] G. Kresse. Ab-initio molecular-dynamics for liquid-metals. *Journal of Non-Crystalline Solids*, 193:222–229, 1995.

[30] P.F. Manicone, P. Rossi Iommetti, and L. Raffaelli. An overview of zirconia ceramics: basic properties and clinical applications. *J Dent*, 35(11):819–26, 2007.

[31] D. Vanderbilt. Soft self-consistent pseudopotentials in a generalized eigenvalue formalism. *Phys Rev B Condens Matter*, 41(11):7892–7895, 1990.

[32] P. Hohenberg and W. Kohn. Inhomogeneous electron gas. *Physical Review*, 136(3B):B864–B871, 1964.

[33] W. Kohn and L.J. Sham. Self-consistent equations including exchange and correlation effects. *Physical Review*, 140(4A):A1133–A1138, 1965.

[34] B. Bondars, G. Heidemane, J. Grabis, K. Laschke, H. Boysen, J. Schneider, and F. Frey. Powder diffraction investigations of plasma sprayed zirconia. *Journal of Materials Science*, 30:1621–1625, 1995.

[35] P. Bouvier, E. Djurado, G. Lucazeau, and T. Le Bihan. High-pressure structural evolution of undoped tetragonal nanocrystalline zirconia. *Physical Review, Serie 3. B - Condensed Matter*, 62:8731–8737, 2000.

[36] A. Togo, F. Oba, and I. Tanaka. First-principles calculations of the ferroelastic transition between rutile-type and cacl2-type sio2 at high pressures. *Phys. rev. B*, 78(13):134106, 2008.

[37] P. Bouvier and G. Lucazeau. Raman spectra and vibrational analysis of nanometric tetragonal zirconia under high pressure. *Journal of Physics and Chemistry of Solids*, 61(4):569–578, 2000.

[38] G.M. Rignanese, F. Detraux, X. Gonze, and A. Pasquarello. First-principles study of dynamical and dielectric properties of tetragonal zirconia. *Physical Review B*, 64(13):134301, 2001.

[39] Q. Fan, F. Wang, H. Zhang, and F. Zhang. Study of zro2 phase structure and electronic properties. *Molecular Simulation*, 34(10-15):1099–1103, 2008.

[40] T. Beck, R. Herzog, O. Trunova, M. Offermann, R.W. Steinbrech, and L. Singheiser. Damage mechanisms and lifetime behavior of plasma-sprayed thermal barrier coating systems for gas turbines part ii: Modeling. *Surface and Coatings Technology*, 202(24):5901–5908, 2008.

[41] J.R. Nicholls, Y. Jaslier, and D.S. Rickerby. Erosion and foreign object damage of thermal barrier coatings. *High Temperature Corrosion and Protection of Materials 4, Pts 1 and 2*, 251-2:935–948, 1997.

[42] C.A. Estrada. New technology used in gas turbine blade materials. *Scientia et Technica*, 4(36), 2007.

[43] J. Yan, A.M. Karlsson, M. Bartsch, and X. Chen. On stresses induced in a thermal barrier coating due to indentation testing. *Computational Materials Science*, 44(4):1178–1191, 2009.

[44] R. Edwin and J. Fuller. Thermal property prediction via finite-element simulations. In *Symposium on Advanced Ceramic Coatings*.

[45] G.S. Upadhyaya. *Cemented Tungsten Carbides - Production, Properties, and Testing*. William Andrew Publishing/Noyes, 1998.

[46] Z. Fang and J.A. Sue. Double cemented carbide composites, 1997.

[47] Z. Fang, G. Lockwood, and A. Griffo. A dual composite of wc-co. *Metallurgical and Materials Transactions A*, 30(12):3231–3238, 1999.

[48] X. Deng, B.R. Patterson, K.K. Chawla, M.C. Koopman, Z. Fang, G. Lockwood, and A. Griffo. Mechanical properties of a hybrid cemented carbide composite. *International Journal of Refractory Metals and Hard Materials*, 19(46):547–552, 2001.

[49] Z. Hashin and S. Shtrikman. A variational approach to the theory of the elastic behaviour of multiphase materials. *Journal of the Mechanics and Physics of Solids*, 11(2):127–140, 1963.

[50] B.D. Agarwal and L.J. Broutman. Three-dimensional finite element analysis of spherical particle composites. *Fibre Science and Technology*, 7(1):63–77, 1974.

[51] P.S. Turner. Thermal-expansion stresses in reinforced plastics. *Journal of National Bureau of Standards*, 37, 1946.

[52] E.H. Kerner. The elastic and thermo-elastic properties of composite media. *Proceedings of the Physical Society. Section B*, 69(8):808, 1956.

[53] R.A. Schapery. Thermal expansion coefficients of composite materials based on energy principles. *Journal of Composite Materials*, 2:24, 1968.

[54] B.W. Rosen and Z. Hashin. Effective thermal expansion coefficients and specific heats of composite materials. *International Journal of Engineering Science*, 8(2):157–173, 1970.

[55] N. Chawla and Y.-L. Shen. Mechanical behavior of particle reinforced metal matrix composites. *Advanced Engineering Materials*, 3(6):13, 2001.

[56] N. Chawla, J. W. Jones, C. Andres, and J. E. Allison. Effect of sic volume fraction and particle size on the fatigue resistance of a 2080 al/sic p composite. *Metallurgical and Materials Transactions A*, 29(11):2843–2854, 1998.

[57] Y.L. Shen, M. Finot, A. Needleman, and S. Suresh. Effective plastic response of two-phase composites. *Acta Metallurgica et Materialia*, 43(4):1701–1722, 1995.

[58] S.A. Langer, E.R. Fuller, and Carter W.C. Oof: an image-based finite-element analysis of material microstructures. *Computing in Science and Engineering*, 3(3):8, 2001.

[59] W.C. Carter, S.A. Langer, and Jr E.R. Fuller. The oof manual: version 1.0, national institute of standards and technology (nist). *NISTIR No. 6256*, 1998.

[60] J.C. Halpin and S.W. Tsai. Environmental factors in composite materials design. Report, Air Force Materials Lab, 1967.

[61] A. Borbly, H. Biermann, and O. Hartmann. Fe investigation of the effect of particle distribution on the uniaxial stressstrain behaviour of particulate reinforced metal-matrix composites. *Materials Science and Engineering: A*, 313(12):34–45, 2001.

[62] H. Shen and C.J. Lissenden. 3d finite element analysis of particle-reinforced aluminum. *Materials Science and Engineering: A*, 338(12):271–281, 2002.

[63] Wilson Instruments NIST C Brale. Brale diamond indenters.

[64] B. Jang and H. Matsubara. Hardness and young's modulus of nanoporous eb-pvd ysz coatings by nanoindentation. *Journal of Alloys and Compounds*, 402(12):237–241, 2005.

[65] D. Cojocaru. *On Numerical Modeling of Cyclically Loaded Structures*. University of Delaware, 2008.